



A quantitative comparison of lightning-induced electron precipitation and VLF signal perturbations

W. B. Peter¹ and U. S. Inan¹

Received 8 November 2006; revised 13 August 2007; accepted 12 September 2007; published 22 December 2007.

[1] VLF signal perturbations recorded on the Holographic Array for Ionospheric/Lightning Research (HAIL) are quantitatively related to a comprehensive model of lightning-induced electron precipitation (LEP) events. The model consists of three major components: a test-particle model of gyroresonant whistler-induced electron precipitation, a Monte Carlo simulation of energy deposition into the ionosphere, and a model of VLF subionospheric signal propagation. For the two representative LEP events studied, the model calculates peak VLF amplitude perturbations within a factor of three of those observed, well within the expected variability of radiation belt flux levels. The phase response of the observed VLF signal to precipitation varied dramatically over the course of the two nights and this variability in phase response is not properly reproduced by the model. The model calculates a peak in the precipitation that is poleward displaced $\sim 6^\circ$ from the causative lightning flash, consistent with observations. The modeled precipitated energy flux ($E > 45$ keV) peaks at $\sim 1 \times 10^{-2}$ (ergs s^{-1} cm^{-2}), resulting in a peak loss of $\sim 0.001\%$ from a single flux tube at $L \sim 2.2$, consistent with previous satellite measurements of LEP events. The precipitation calculated by the model is highly dependent on the near-loss-cone trapped radiation belt flux levels assumed, and hence our main objective is not to compare the model calculations and the VLF signal observations on an absolute basis but is rather to develop metrics with which we can characterize the VLF signal perturbations recorded on HAIL in terms of the associated precipitation flux. Metrics quantifying the ionospheric density enhancement (N_{ILDE}) and the electron precipitation (Γ) along a VLF signal path are strongly correlated with the VLF signal perturbations calculated by the model. A conversion ratio Ψ , relating VLF signal amplitude perturbations (ΔA) to the time-integrated precipitation (100–300 keV) along the VLF path ($\Psi = \Gamma/\Delta A$), of $1.2 \pm 0.3 \times 10^{10}$ (el m^{-1}/dB) is suggested for precipitation events of similar location and characteristics to those examined. The total precipitation (100–300 keV) induced by one of the representative LEP events is estimated at $\sim 1.8 \pm 0.4 \times 10^{16}$ electrons, calculated directly from the conversion ratio Ψ and observations of VLF signal perturbations.

Citation: Peter, W. B., and U. S. Inan (2007), A quantitative comparison of lightning-induced electron precipitation and VLF signal perturbations, *J. Geophys. Res.*, 112, A12212, doi:10.1029/2006JA012165.

1. Introduction

[2] Subionospheric very low frequency (VLF) signals have long been used to detect transient perturbations of the upper atmosphere associated with lightning-induced electron precipitation (LEP) events [e.g., Helliwell *et al.*, 1973; Inan *et al.*, 1985; Inan and Carpenter, 1986]. This paper examines two representative LEP events detected via VLF remote sensing during March 2001 and compares the VLF signal amplitude and phase perturbations observed with a comprehensive model of lightning-induced electron precipitation.

[3] Lightning discharges indirectly produce localized ionospheric disturbances through lightning-induced bursts of precipitation of energetic radiation belt electrons. LEP events are produced by the fraction of the VLF energy radiated by lightning discharges that escapes into the magnetosphere and propagates therein as a whistler-mode wave (Figure 1). The whistler-mode wave interacts with trapped radiation belt electrons via cyclotron resonance, leading to pitch angle scattering of the electrons, causing some of those close to the loss cone to precipitate into the lower ionosphere where they produce secondary ionization. Past work has distinguished two types of VLF perturbation signatures associated with electron precipitation induced by “ducted” and “nonducted” whistler waves. In the presence of field-aligned ducts of enhanced ionization in the magnetosphere, “ducted” whistler waves propagate along the enhanced duct [Burgess and Inan, 1993]. Precipitation of

¹Space Telecommunications and Radioscience Laboratory, Stanford University, Stanford, California, USA.

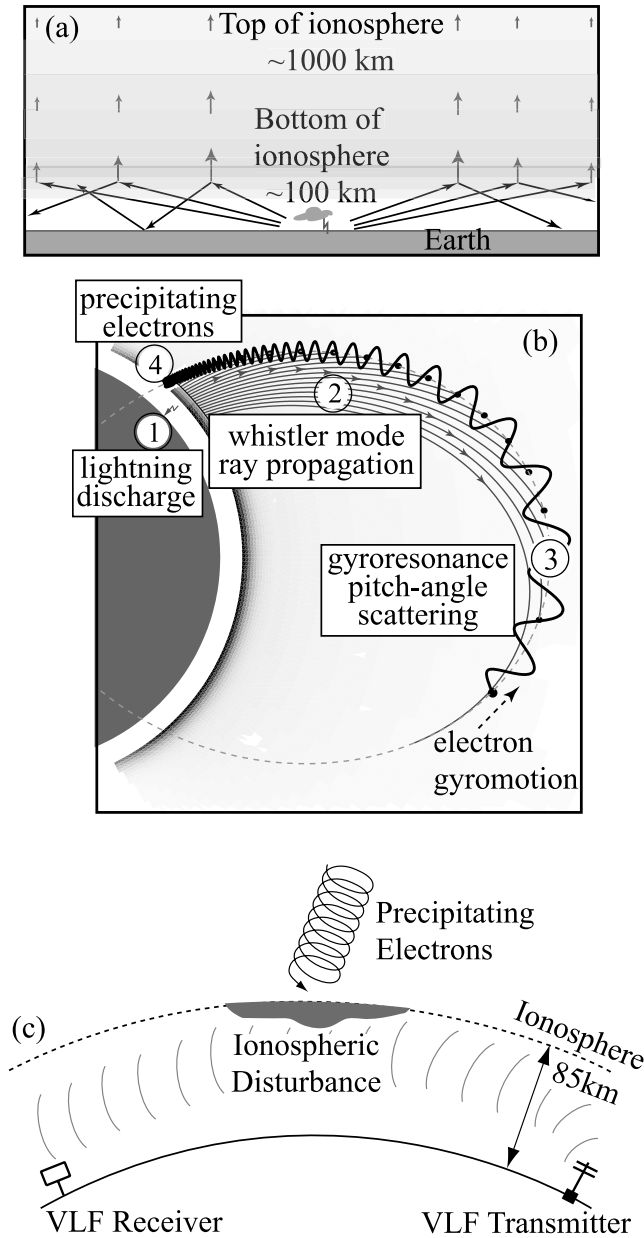


Figure 1. Lightning-induced electron precipitation (LEP) events, showing (a) illustration of a lightning discharge radiating VLF wave energy, a portion of which is coupled into the magnetosphere and propagates therein as a whistler wave, and (b) illustration of the wave-particle interaction process: (1) lightning discharge occurs, (2) propagation of the whistler wave in the magnetosphere, (3) wave-particle interaction near the equatorial plane scatters the pitch angle of a fraction of the trapped energetic radiation belt electrons into the loss cone, and (4) electrons precipitate into the dense upper atmosphere. (c) Precipitating electrons produce secondary ionization, which in turn changes the electrical conductivity of the upper boundary of the Earth-ionosphere waveguide and perturbs the VLF wave propagating underneath (adapted from *Lauben et al.* [1999]).

energetic electrons can also be caused by obliquely propagating “nonducted” whistlers [*Johnson et al.*, 1999], affecting a region of the radiation belts of several degrees in invariant latitude and geomagnetic longitude, and resulting in precipitation of electrons over ionospheric regions of ~ 1000 km in lateral extent. Nonducted whistler wave energy can also magnetospherically reflect (MR whistlers), resulting in longer wave lifetimes and an increase in total precipitation [*Bortnik et al.*, 2003a]. The two LEP events examined in this paper were previously included in a statistical study of LEP events [*Peter and Inan*, 2004] that classified these LEP events as nonducted, due to the large spatial extent of the affected ionospheric regions and the increasing measured onset delay of the disturbance with latitude.

[4] The precipitating energetic electrons (~ 50 to 500 keV) cause secondary ionization via impact with atmospheric constituents, altering the conductivity of the *D* region of the ionosphere. This ionospheric disturbance in turn changes the amplitude and/or phase of VLF transmitter signals propagating in the Earth-ionosphere waveguide on great circle paths (GCPs) that pass through or near the localized disturbance [*Poulsen et al.*, 1993]. The amplitude and phase of VLF transmitter signals observed at any point can thus be used to measure the spatial and temporal characteristics of localized disturbances in the lower ionosphere.

[5] Both theoretical [*Bortnik et al.*, 2003a; *Abel and Thorne*, 1998a, 1998b] and experimental works [e.g., *Burgess and Inan*, 1993; *Voss et al.*, 1998] suggest that wave energy injected by lightning discharges is an important contributor to the loss rates of radiation belt particles, especially at lower *L*-shells ($L \sim 3$). The role of lightning-injected whistlers in the loss-rate of energetic radiation-belt electrons was estimated by *Abel and Thorne* [1998a, 1998b], who calculated the scattering rates and electron lifetimes due to plasmaspheric hiss, coulomb interactions, whistlers, and anthropogenic VLF transmitters and concluded that in the vicinity of the slot region whistlers are indeed important drivers of pitch-angle scattering. *Bortnik et al.* [2003a] provided a first-order estimate of the distribution of MR whistler wave energy as a function of *L*-shell, using ray tracing and incorporating Landau damping of the whistler wave. The results indicated that MR whistler energy deposition is maximized at the location of the slot region, suggesting that MR whistlers may play a more significant role than previously assumed in the formation and maintenance of the slot region.

[6] Lightning may additionally contribute to electron losses via generation of plasmaspheric hiss and drift loss cone enhancements. *Green et al.* [2005] reported evidence of an association between lightning and plasmaspheric hiss. Drift-loss cone enhancements of >150 keV and >500 keV electrons on SAMPEX spacecraft, in association with thunderstorm activity, were interpreted as precipitation driven by MR whistlers [*Blake et al.*, 2001]. Also relevant to this report is the work of *Rodger et al.* [2004], which modeled satellite and ground-based observations of electron precipitation event onset and decay and its effects in the ionosphere by examining associated VLF signal perturbations.

[7] However, the lack of quantitative measurements of lightning-induced precipitations events makes it difficult to

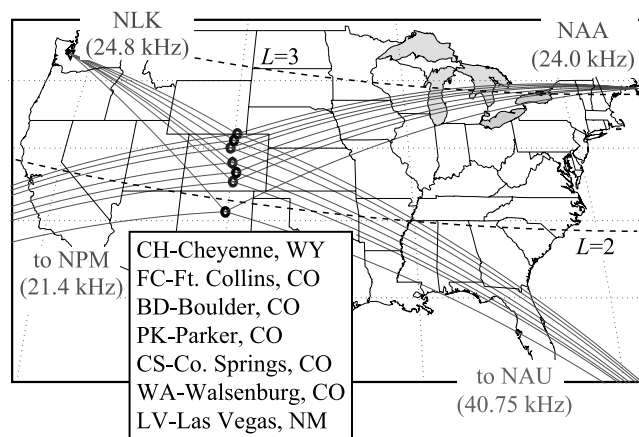


Figure 2. The location of the Holographic Array for Ionospheric/Lightning Research (HAIL) VLF receivers, with the great circle paths (GCPs) of the subionospherically propagating VLF signals shown as solid lines. The names of the receiver locations are shown in the box.

confirm the predictions of *Abel and Thorne* [1998a, 1998b] and *Bortnik et al.* [2003a], which are based on assumptions concerning the precipitation fluxes driven by individual whistler-mode wave bursts originating in particular lightning discharges. Through a comparison of VLF experimental observations of LEP events with a comprehensive model of lightning-induced electron precipitation and the resulting ionospheric disturbance, we attempt in this paper to quantitatively measure the precipitation associated with two representative LEP events. Our results demonstrate the usefulness of VLF remote sensing in accurately characterizing precipitation events and resulting ionospheric electron density enhancements.

[8] This paper consists of two major components. The first is the application of a modeling framework to two representative LEP events. This modeling framework is the most comprehensive model to date in terms of quantitative interpretation of VLF signal perturbations associated with nonducted lightning-induced electron precipitation. The VLF amplitude and phase perturbations calculated by the model are directly comparable to the VLF signal observations. However, recognizing that the precipitation is highly dependent on the near-loss-cone trapped radiation belt flux levels (that are known to be highly variable), our main objective is not to compare model calculations (for assumed trapped particle flux levels) with the HAIL VLF signal observations on an absolute basis but is rather to develop metrics with which we can characterize the VLF signal perturbations in terms of the associated precipitation flux. The second major component of this paper is thus the development of a methodology by which we can estimate the total precipitation induced by a single lightning flash, using only the developed conversion ratios and observations of VLF signal perturbations.

2. Description of the Two Case Studies

[9] We consider two LEP events detected by the Holographic Array for Ionospheric/Lightning Research (HAIL), a set of VLF receivers spread along the eastern side of the

Rocky Mountains (Figure 2). The HAIL array continuously monitors the amplitude and phase of coherent and subionospherically propagating VLF transmitter signals operated by the United States Navy in Washington (NLK at 24.8 kHz), Maine (NAA at 24.0 kHz), Hawaii (NPM at 21.4 kHz), and Puerto Rico (NAU at 40.75 kHz). A $1.7 \times 1.7 \text{ m}^2$ magnetic loop antenna connected to a preamplifier is used to detect the VLF signal at all receivers. The broadband VLF signal is bandpass filtered to a range of 9–45 kHz and then is digitized at a rate of 100 kHz with 16-bit resolution, with triggers provided by GPS timing. Each receiver digitally down-converts the individual VLF transmitter signals and records the demodulated amplitude and phase with 20 ms resolution.

[10] The two events are chosen based on their clear VLF signatures in the HAIL data, their occurrence at a similar time of night and year, and the existence of a previous statistical work that included both events [*Peter and Inan, 2004*]. Figure 3 shows 3-min records of the NAA and NAU VLF signal amplitudes received at the HAIL sites in operation during each case, with a map showing the location of the relevant HAIL sites and GCPs. The event perturbation magnitude (ΔA) of the LEP event is measured for each VLF signal and refers to the change in amplitude, measured in dB, from the ambient levels prior to the event to the maximum (or minimum) levels reached during the event. The associated phase change $\Delta\phi$ is also measured in a similar manner. Note that the paths with the peak perturbation (i.e., NAA-WA for Case 1 and NAU-PK for Case 2) are poleward displaced from the causative flash location, typical of nonducted LEP events [*Johnson et al., 1999*]. No perturbation is detected on the northernmost and southernmost GCPs. The full latitudinal extent of the ionospheric perturbation region is captured for both cases.

[11] The National Lightning Detection Network (NLDN) provides the timing, location and peak current of causative cloud-to-ground (CG) lightning discharges within the continental United States with 1-ms resolution [*Cummins et al., 1998*]. The correlation of the specific causative lightning flash in the NLDN data with the VLF perturbation observed on HAIL was determined by *Peter and Inan* [2004]. The first case was induced by a +133.3 kA CG flash, located in northern Texas, at 07:13:20.68 on 24 March 2001. The second case was induced by a –155.1 kA CG flash, located ~300 km southeast of the Case 1 flash, at 07:09:47.86 UT on 28 March 2001. Table 1 lists the relevant parameters for the two cases.

3. Description of Model

[12] The theoretical model framework used in this paper is made up of three major components: a model of whistler-induced electron precipitation [*Bortnik et al., 2006a*], a Monte Carlo simulation of the energy deposition into the ionosphere resulting from the calculated precipitation flux [*Lehtinen et al., 2001*], and a model of VLF subionospheric signal propagation that takes into account the disturbed ionospheric density profiles [*Chevalier and Inan, 2006*]. The model outputs VLF signal perturbations that are directly compared to the VLF signal perturbations observed on the HAIL array. A block diagram of the framework used to model the two representative LEP events is shown in Figure 4.

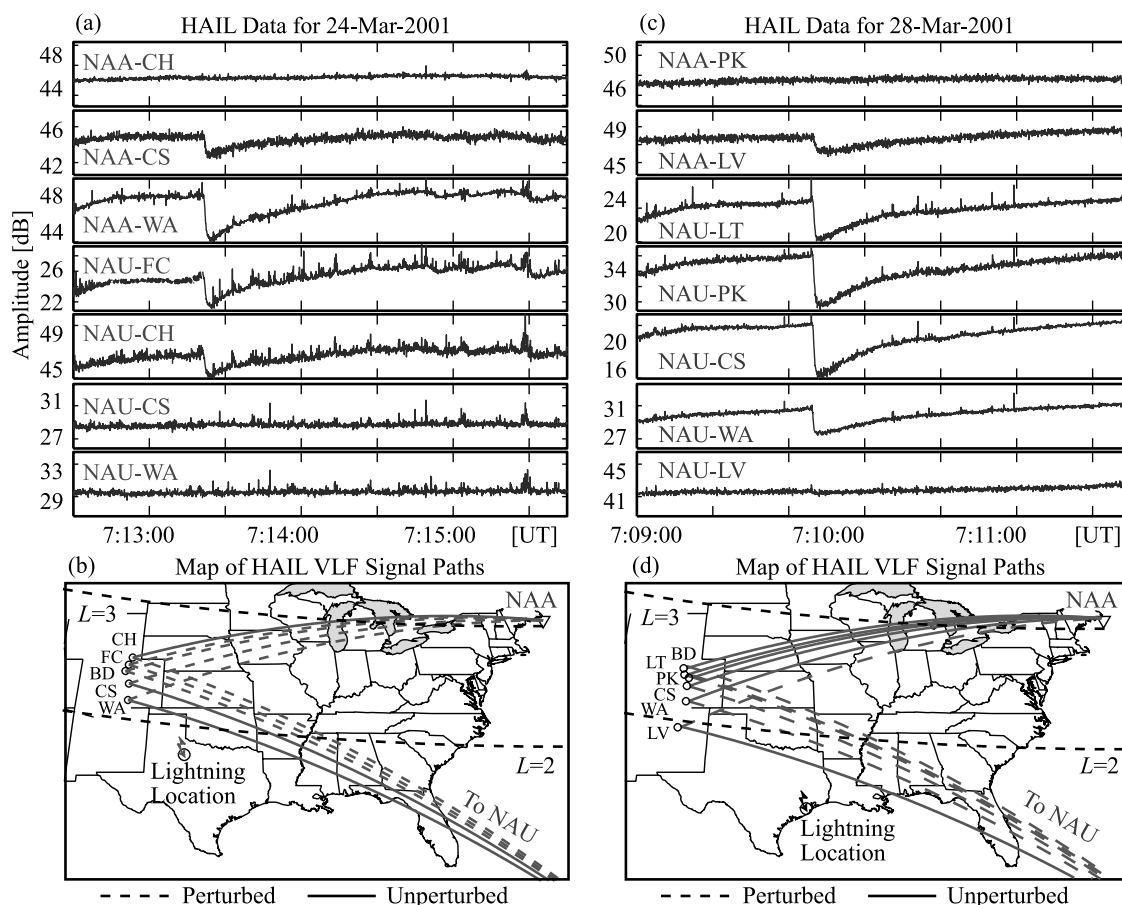


Figure 3. VLF signatures of LEP events, showing (a) case 1, an LEP event observed on 24 March 2001. A 3-min record of the NAA and NAU signal amplitude (in dB) at five HAIL sites is shown on a 6-dB scale. Also shown is (b) a map showing the GCPs from the two VLF transmitters to each HAIL site. An associated VLF perturbation is detected on the dashed GCPs, and no measurable perturbation is detected on the solid GCPs. Also shown is (c) case 2, an LEP event observed on 28 March 2001. A 3-min record of the received NAA and NAU signal amplitude at six HAIL sites is shown on a 6-dB scale. Finally shown is (d) a map showing the perturbed GCPs (dashed lines) and those GCPs with no measurable perturbation (solid lines). For both events, the full latitudinal extent of the LEP precipitation region is captured.

3.1. Whistler-Induced Precipitation Model

[13] The lightning discharge is modeled in the same manner as *Bortnik et al.* [2002], using the expression of *Uman* [1984, p. 61]. The lightning location and peak vertical current are taken from NLDN data (Table 1), with the lightning location transformed to simple dipole geomagnetic coordinates. The power spectral density is directly proportional to the square of the peak vertical current and falls off with the square of distance from the lightning location. The computed wave power density is translated to

~ 1000 km altitude, the point of injection of the rays, by properly attenuating it according to an absorption factor taken from *Helliwell* [1965, Figures 3–35]. The magnitude of the whistler-mode wave magnetic field is directly proportional to the peak vertical current of the lightning flash. As detailed by *Bortnik et al.* [2006a], the frequency spectrum of the wave packet is broadly peaked between 2 and 6 kHz and for the purposes of ray tracing is discretized into 130 frequency components spaced approximately logarithmically between 200 Hz and 60 kHz. Forty-one rays are

Table 1. Input Parameters for the Two Representative LEP Events^a

Case	Date	Time	Latitude	Longitude	Peak Current	L_{pp}
1	24 Mar 2001	713:20.68	33.34°N	100.06°W	+133.3 kA	3.45
2	28 Mar 2001	709:47.86	30.19°N	95.73°W	−155.1 kA	2.84

^aThe lightning time (in UT), location (in geographic latitude and longitude), and peak current (in kA) are taken from the NLDN data. The plasmopause locations (L_{pp}) are estimated from EUV IMAGE data (courtesy of M. Spasojevic (private communication, 2006)).

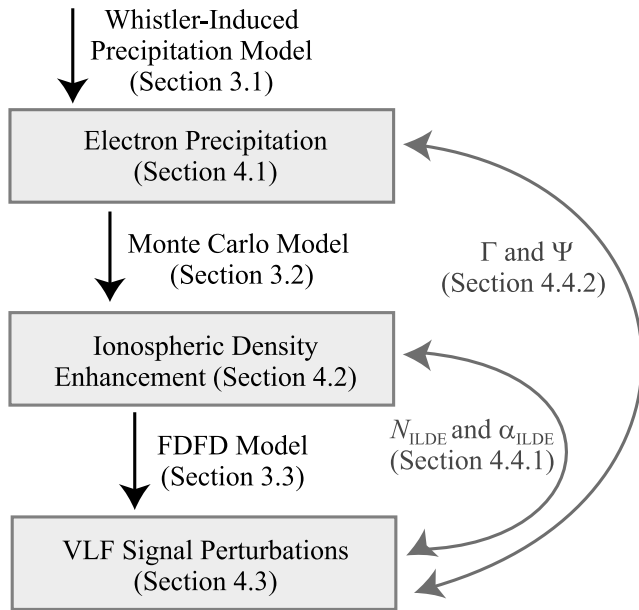


Figure 4. Block diagram showing the framework of the LEP model. Also shown is the relationship of the metrics and conversion ratios to the framework. The relevant section for each component is indicated.

injected per frequency component, spaced every 0.5 degrees in latitude and covering twenty degrees of latitude centered at the source lightning latitude, resulting in a total of 5330 traced rays. We then interpolate every 0.01 degrees in injection latitude and every 1 Hz in frequency for a total of ~ 120 million interpolated ray paths. The wave normal vectors input into the model are initially vertical, assuming no horizontal density gradients in the ionosphere, consistent with past work [Thorne and Horne, 1994; Lauben et al., 1999; Bortnik et al., 2006a]. The horizontally stratified sharp edge of the lower ionosphere provides a high refractive index gradient in the vertical direction, so the wave normal angle of the whistler wave which couples upward is pulled toward the local vertical direction. Bortnik et al. [2002] found that horizontal density gradients in the ionosphere could focus lightning-generated whistler waves in latitude. The effects of horizontal density gradients in the ionosphere are not included in the model used in this work and may influence the spatial extent of the precipitation region. The initial whistler wave packet has a pulse length of ~ 200 ms [Bortnik et al., 2006a], consistent with a typical lightning waveform [Uman, 1984, chap. 4].

[14] Whistler wave propagation in the magnetosphere is simulated using the Stanford VLF ray tracing code [Inan and Bell, 1977], which is essentially an implementation of a two-dimensional (2-D) integration of Haselgrove's equations [Haselgrove, 1954]. A tilted, centered dipole geomagnetic field model is used, with the 2-D ray tracing done in the magnetic dipole meridian plane. The effects of Landau damping are included using the theoretical formulation of Brinca [1972] in conjunction with typical suprathermal electron distributions observed by the HYDRA instrument on the Polar spacecraft [Bell et al., 2002].

3.1.1. Plasmaspheric Density

[15] Variations in the cold plasmaspheric electron density can significantly influence the propagation of lightning-generated whistler waves. Steeper radial gradients in plasmaspheric density constrain the wave energy to lower L -shells. Higher absolute values in plasmaspheric density slow the propagation of whistler waves, with the speed of propagation being approximately inversely proportional to the square root of density [Park, 1972]. The equatorial density profile adapted for our use (Figure 5a) is based on the work of Tarcsai et al. [1988]. The Carpenter and Anderson [1992] model (also shown for reference) is intended for use for $L > 2.5$. Using the equatorial density based on Carpenter and Anderson [1992], the model calculates the electron precipitation to be displaced significantly further poleward from the lightning flash than that which is observed on the HAIL array [Bortnik et al., 2006b]. Using the equatorial density based on Tarcsai et al. [1988], the model predictions suggest a region of precipitation located in a region consistent with the observations made on HAIL, suggesting that the Tarcsai et al. [1988] model estimates the plasmaspheric density gradients at lower L -shells more accurately than Carpenter and Anderson [1992]. This result is expected since the Carpenter and Anderson [1992] model is largely based on in situ and whistler data from relatively higher L -shells, while the Tarcsai et al. [1988] model is at least partly based on observations of whistlers at very low latitudes. The dependence of the poleward displacement on the plasmaspheric density gradients suggests the possible use of VLF remote sensing of precipitation events as an indicator of the radial variation in plasmaspheric density.

[16] Geomagnetic activity increased in the later half of March 2001, resulting in relatively compressed plasmapause locations of $L_{pp} \sim 3.45$ for Case 1 and $L_{pp} \sim 2.84$ for Case 2 (Table 1). The plasmapause locations are estimated from EUV IMAGE data (courtesy of M. Spasojevic (private communication, 2006)). The variation of electron number density along the field lines is calculated using the diffusive equilibrium model of Angerami and Thomas [1964]. The presence of plasmaspheric ducts of enhanced electron density can be used in the model, but previous modeling has shown that the majority of whistler wave energy is not trapped by the ducts [Bortnik et al., 2003b], and accordingly no plasmaspheric ducts are included.

3.1.2. Trapped Energetic Flux

[17] The precipitated flux induced by lightning-generated whistlers is highly sensitive to the flux levels and initial pitch angle distribution of the trapped electron population, especially near the edge of the bounce loss cone [Inan et al., 1982, 1989]. The trapped energetic flux levels we use (Figure 5b) are based on the AE8 radiation belt model [Vette, 1991]. However, the trapped flux levels for $L > 2$ are known to vary considerably with time, especially during geomagnetically active periods such as those during the two cases considered here. Given this variability of energetic flux levels with L -shell, differences between the model and observation are expected in terms of the spatial characteristics (e.g., L -dependence) and the absolute magnitude (i.e., flux) of the precipitation.

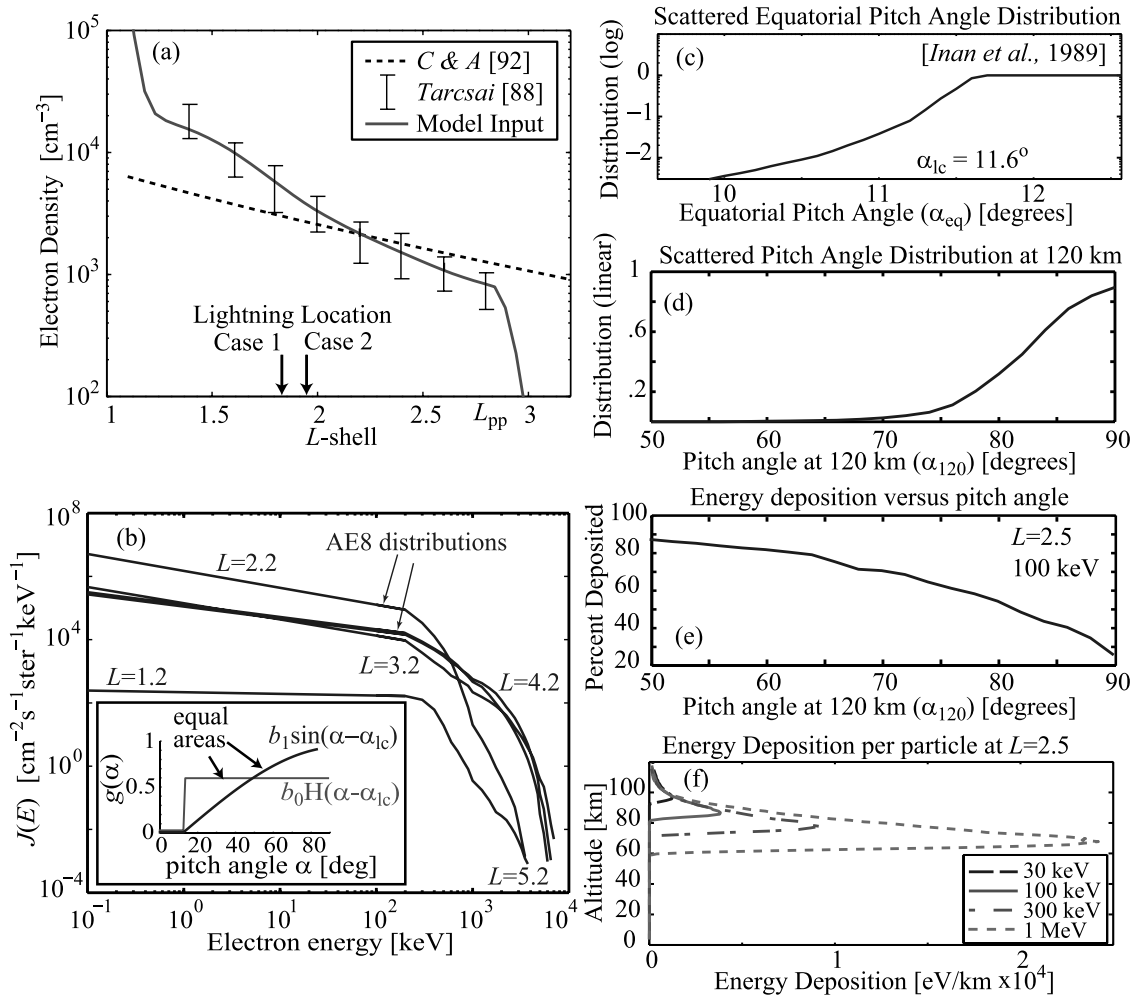


Figure 5. Model input parameters, showing (a) equatorial cold plasmaspheric electron density. The Tarcsei *et al.* [1988] and Carpenter and Anderson [1992] models are shown for reference. Also shown is (b) trapped energetic electron flux levels based on the AE8 model [Vette, 1991] at $L = 1.2, 2.2, 3.2, 4.2,$ and 5.2 . The inset shows a “square” and “sine” pitch-angle distribution. H denotes the Heaviside step function. Figure modified from Bortnik [2004]. Finally shown is (c) scattered equatorial pitch angle distribution for precipitating particles at $L = 2.5$, taken from Inan *et al.* [1989], (d) the scattered pitch angle distribution mapped down to 120 km, assuming conservation of the electron energy and first adiabatic invariant, (e) percent of energy deposited into the atmosphere for a 100 keV particle as a function of pitch angle at 120 km and $L = 2.5$, and (f) energy deposition per particle, as a function of altitude, for electrons of four different energies at $L = 2.5$. The precipitation is assumed to have the pitch angle distribution given in Figure 5d.

[18] In fact, the NOAA-POES satellites observed a dramatic increase in the trapped energetic flux levels near the loss cone during the later half of March 2001 [Peter and Inan, 2004]. The AE8 radiation belt model assumes a “sine” pitch-angle distribution, but to account for the increase in particle flux near the loss cone observed by the NOAA-POES satellites, an initial unperturbed “square” pitch angle distribution was input into the model. Modeling results using a “sine” pitch angle distribution (not shown) predicted VLF signal perturbations two orders of magnitude less than those observed, suggesting that the pitch angle distribution near the loss cone was more similar to that represented by the “square” distribution during the two cases. In this context it is important to note that for the parameters of typical whistler wave intensities and in the

inner radiation belt and slot regions, the wave-induced scattering involves basically weak diffusion (or small angle scattering) and that the precipitation fluxes are thus approximately proportional to the flux levels near the loss cone edge [Inan *et al.*, 1982, 1989; Bortnik *et al.*, 2002].

[19] Hence the scale of the precipitation predicted by the model is dependent on an unknown quantity, that is, the trapped flux levels near the edge of the loss cone. Therefore we expect differences between the VLF signal observations and those calculated by the model. However, the comparison of the modeling results with observations provides information about the degree to which the model accurately captures the physical processes involved. Furthermore, by assuming that the precipitation calculated by the model is representative of LEP events, we can develop metrics to

quantitatively relate observed VLF perturbation signatures to associated electron precipitation.

3.1.3. Pitch Angle Scattering

[20] The pitch angle scattering of energetic particles into the loss cone by whistler wave cyclotron resonance is calculated according to the work of *Bortnik et al.* [2006a]. This model accounts for the coherence and finite duration of the whistler wave packet and provides temporal detail about the precipitation not obtained via a steady-state (bounce-averaged) diffusion analysis. Furthermore, the *Bortnik et al.* [2006a] model is the most current in terms of properly accounting for the oblique propagation, magnetospheric reflection, and Landau damping of the whistler wave. The rate of pitch angle change of a particle moving through an oblique whistler wave field is determined from the relativistic gyroaveraged equations of motion for a general harmonic resonance [*Bell*, 1984; *Jasna*, 1993], with the first five resonant modes considered [*Bortnik et al.*, 2006a]. The pitch angle scattering of energetic electrons is dependent on the k -vector angular distribution (with respect to the Earth's magnetic field) of the whistler-mode wave. As *Peter and Inan* [2004] concluded that the LEP events considered in this report were induced by whistler waves that are predominantly nonducted, we assume the model accurately captures the k -vector distribution of the whistler-mode waves. The parallel and perpendicular velocities are approximated to first order so that nonlinearities due to wave forces are not included. Typical errors between the analytical solution used and the full solution are $<1\%$ for near-resonant particle velocities [*Bortnik et al.*, 2006a].

[21] The combination of the ray tracing simulation and the scattering calculation returns precipitation flux as a function of L -shell and time at the geomagnetic longitude of the source lightning flash. All particles scattered into the loss cone are counted as precipitation flux, with the resulting energy deposition into the atmosphere determined as described in section 3.2. It is assumed that there are no longitudinal gradients in ionospheric or plasmaspheric density and the precipitation flux is simply scaled according to the falloff in lightning-generated electromagnetic energy with distance from the flash longitude [*Bortnik et al.*, 2003b, equation (1)], allowing the determination of precipitation flux as a function of longitudinal displacement from the source lightning longitude [*Bortnik et al.*, 2006b, Figure 6].

3.2. Monte Carlo Deposition

[22] The calculated precipitation flux (determined as a function of incident particle energy) is subsequently input into a Monte Carlo simulation of the penetration of energetic electrons into the ionosphere to determine the energy deposition (and secondary ionization production) as a function of L -shell and altitude [*Lehtinen et al.*, 2001]. While it would be possible to calculate a specific perturbed pitch angle distribution for different particle energies, locations, and times, a single perturbed pitch angle distribution is assumed for all energies, times, and locations to simplify the calculations. The perturbed pitch angle distribution (Figure 5c) used in all of our modeling is thus based on the modeling work of *Inan et al.* [1989]. Figure 5d shows this pitch angle distribution mapped down to 120 km altitude, the point of injection into the Monte Carlo simulation. The pitch angle distribution is mapped down

to 120 km assuming conservation of the electron energy and the first adiabatic invariant and is normalized to match the distribution of Figure 5c. Figure 5e shows the dependence of the percentage of the particle energy deposited into the atmosphere on particle pitch angle. Particles nearly perpendicular to the geomagnetic field at 120 km are more likely to be reflected (i.e., backscattered) prior to losing all their energy in collisions with atmospheric constituents, resulting in lower average energy deposition.

[23] It should be noted that the *Inan et al.* [1989] pitch angle distribution is calculated from a model of ducted whistler induced precipitation, rather than nonducted whistler induced precipitation. However, given that the initial, unperturbed pitch angle distribution is unknown (assumed here to be square) and that particles are unlikely to be scattered far into the loss cone (i.e., the wave-induced scattering involves basically weak diffusion or small-angle scattering for both ducted and nonducted interactions), the use of the *Inan et al.* [1989] distribution provides a sufficiently accurate representation of the effect of the precipitation events on the ionosphere.

[24] The altitude of energy deposition in the ionosphere is highly dependent on the energy of the precipitating particle. Figure 5f shows the energy deposition as a function of altitude for particles of four different energies precipitated at $L = 2.5$, using the pitch angle distribution shown in Figure 5d. Higher-energy particles by definition deposit more total energy per particle, and they deposit relatively more energy at lower altitudes [*Banks et al.*, 1974]. Also note that particles in the 100–300 keV range deposit the majority of their energy at ~ 85 km, the inferred nighttime reflection height for VLF signals [*Wait and Spies*, 1964]. The total energy deposited into the atmosphere (integrated over altitude) is less than the energy of the corresponding precipitating electron, since the average fraction of energy deposited is dependent on the initial particle pitch angle (Figure 5e).

[25] Using the precipitation flux (a function of L -shell and longitude) as an input for the Monte Carlo simulation, a three-dimensional map (altitude, longitude, and L -shell) of energy deposition is determined. The resulting electron density enhancement is calculated assuming one ion-electron pair is produced per 35 eV deposited [*Rees*, 1963]. It should be noted that relaxation processes are not considered in the model and typically occur on the timescales of 10–100 s in the midlatitude D -region ionosphere [*Glukhov et al.*, 1992]. As the majority of the precipitation for the two cases occurs within the first 5 s, it is assumed the relaxation of the ionosphere does not significantly change the results presented.

[26] The electron density enhancement is added to an ambient nighttime density profile (profile 2 in Figure 4 of *Pasko and Inan* [1994]) to give the modified ionospheric density profile as a function of L -shell (sampled every 0.1 L), longitude (sampled every 0.5 degrees), and altitude (sampled every 1 km). The variation in ionospheric density along the GCP of the propagating VLF signal is then input into a model of VLF signal propagation.

3.3. VLF Signal Propagation

[27] The ionospheric density along each GCP monitored by the HAIL array is input into a new Finite Difference

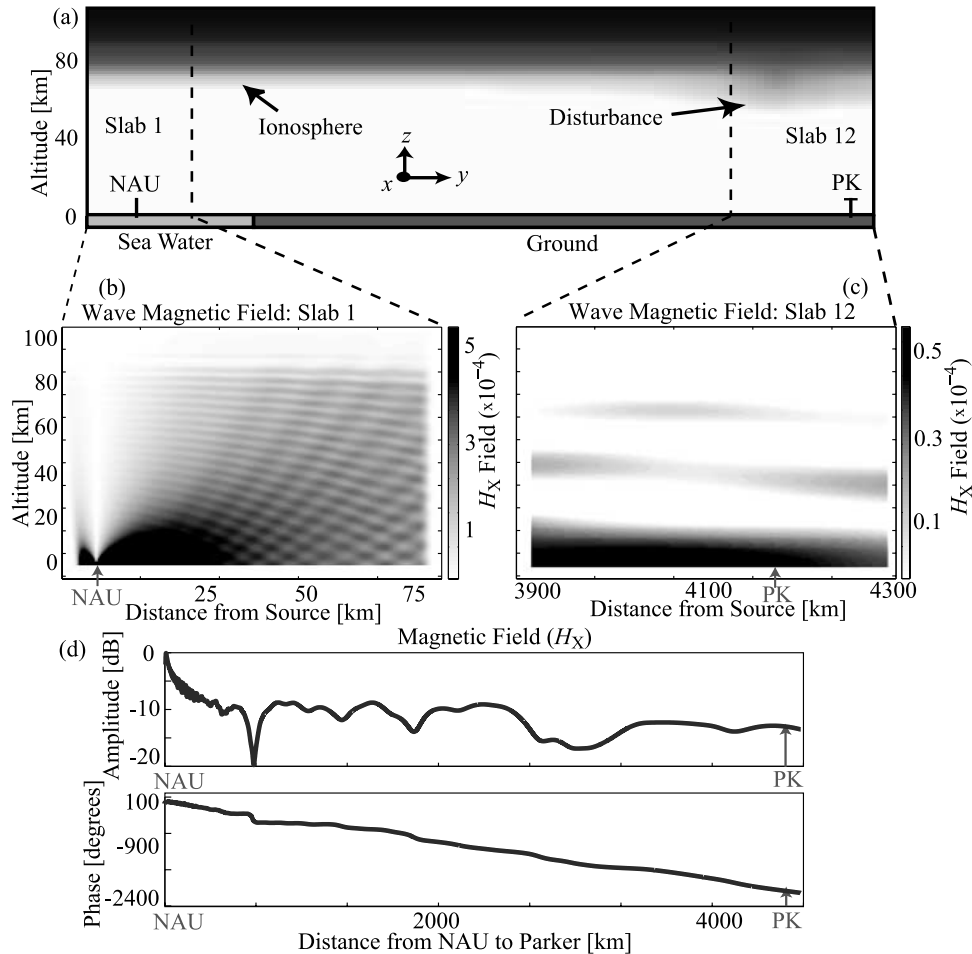


Figure 6. Model of VLF signal propagation, showing (a) schematic of the finite difference frequency domain (FDFD) fully electromagnetic model of VLF signal propagation, showing the division of the GCP into segments, (b) 2-D image of the wave magnetic field H_x (oriented perpendicular to the path) near the NAU transmitter, measured in dB with respect to the magnetic field at the transmitter, (c) magnetic field H_x near the Parker (PK) receiver (note the larger region and different color scale than in Figure 6b), and (d) magnetic field H_x amplitude (top) and phase (bottom) along the GCP from NAU to PK, with respect to the wave magnetic field at the transmitter, for an ambient ionosphere.

Frequency Domain (FDFD) model of subionospheric VLF signal propagation [Chevalier and Inan, 2006] to quantitatively relate the ionospheric density enhancements to the measured VLF signal perturbations. The model consists of a 2-D grid in cylindrical coordinates taking into account the curvature of the Earth. The input parameters into the magnetized plasma equations [Lee and Kalluri, 1999] are static magnetic field, ground conductivity, electron-neutral collision frequency, and electron density. For the static magnetic field a tilted dipole model is used [Walt, 1994, p. 27–31]. The model incorporates variances in the electromagnetic properties of the ground and seawater where relevant in the region modeled. The electron-neutral collision frequency profile can be varied along the path; for the results shown here a single profile $\nu(z) = 4.303 \times 10^{11} e^{-0.1622z}$ is used, where ν is in s^{-1} and z is in kilometers [Chevalier and Inan, 2006]. The electron density profile is obtained from the Monte Carlo calculations (after addition to the ambient profile). Owing to computational resource constraints, the GCP is broken up into segments (Figure 6a),

with each segment surrounded with a perfectly matched layer (PML) boundary condition to absorb any outgoing waves [Chevalier and Inan, 2006]. Making use of the total field/scattered field methodology [Taflove and Hagness, 2000], the VLF signal is then propagated in the forward direction from segment-to-segment along the path.

[28] Figure 6b shows the magnitude of the H_x magnetic field (oriented perpendicular to the path of propagation) for the 40.75 kHz NAU signal. The VLF signal reflects at ~ 85 km, the nighttime reflection height of the D -region ionosphere, and is guided along the Earth-ionosphere waveguide. As the wave propagates along the path, the higher-order modes rapidly decay, leaving only the lower order modes at the location of the receiver (Figure 6c). As the HAIL receivers measure the wave magnetic field strength at the surface of the Earth, we calculate the amplitude and phase of the wave magnetic field along the entire path at the surface of the Earth (Figure 6d). Owing to the decay of the higher order modes with distance, the amplitude at the HAIL receiver locations is relatively stable. The effect of

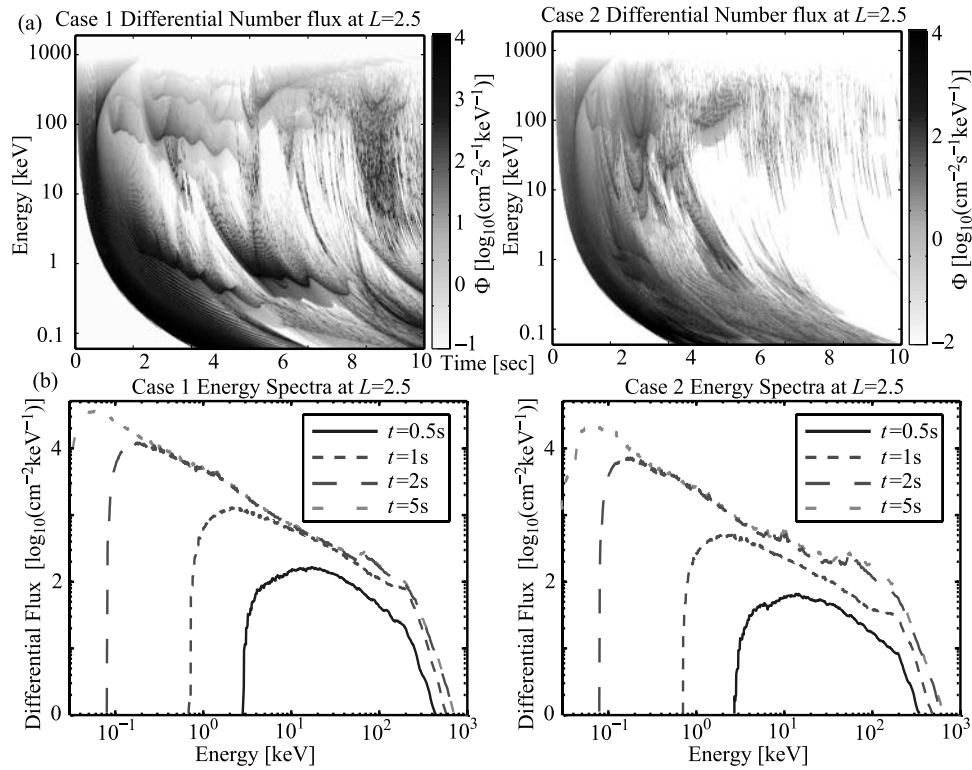


Figure 7. Differential number flux, showing (a) differential flux as a function of time and energy at $L = 2.5$ from 10 eV to 1 MeV for both cases. The higher-energy precipitation is induced by cyclotron resonance pitch angle scattering by the propagating whistler wave. The effects of the magnetospheric reflection of the whistler wave are included, and the resulting precipitation varies with L -shell (sampled every $0.1 L$). Time equals zero at the time of the causative lightning flash. Also shown is (b) time-integrated differential flux as a function of energy integrated over 0.5, 1, 2, and 5 s at $L = 2.5$ for both cases.

the ionospheric disturbance on the magnetic field strength at the location of each HAIL receiver is calculated and compared with the VLF signal perturbations observed.

4. Results

4.1. Precipitation Flux

[29] As detailed in section 3.1, the whistler-induced precipitation model calculates differential flux as a function of time, energy, and L -shell. Figure 7 shows the differential flux at $L = 2.5$ and at the longitude of the lightning flash for both cases. Lower-energy precipitation, associated with Landau resonance between the whistler wave and the energetic electrons, persists for longer times (~ 10 s) than the higher-energy precipitation (>30 keV), induced as a result of cyclotron resonance pitch angle scattering by the propagating whistler wave. The majority of the high-energy precipitation occurs within the first 5 s. The duration of precipitation is lengthened by the presence of magnetospherically reflecting (MR) whistlers, consistent with past modeling [Bortnik *et al.*, 2003b], and is considerably longer than that assumed in past works [Rodger *et al.*, 2002]. The compressed plasmopause ($L_{pp} \sim 2.84$ for Case 1 and $L_{pp} \sim 3.45$ for Case 2) results in guiding of whistler wave energy at the steep plasmopause gradient [Inan and Bell, 1977].

[30] Integrating the differential number flux (Figure 7a) over time gives the energy spectrum of the total precipitated

flux through 0.5, 1, 2, and 5 s (Figure 7b). Significant precipitation of lower energy (<10 keV) electrons continues through 5 s. The majority of the higher-energy electron precipitation (>10 keV), those energies most important in altering the D -region ionosphere (Figure 5f), occurs within the first 2 s.

[31] As we use the same radiation belt model (section 3.1.2) as that used in the model of Bortnik *et al.* [2006a, 2006b], we expect the precipitation calculated by our model runs to be comparable to the results reported by Bortnik *et al.* [2006a, 2006b]. To directly compare our results with Bortnik *et al.* [2006a, 2006b], we calculate the precipitated energy flux ($E > 45$ keV), which peaks at $\sim 1 \times 10^{-2}$ [ergs $\text{s}^{-1} \text{cm}^{-2}$] at $L \sim 2.4$ for Case 1 and $L \sim 2.2$ for Case 2. This peak flux is approximately 10 times larger than the peak energy flux calculated for LEP events in the work of Bortnik *et al.* [2006b]. However, this difference is simply due to the differences in the intensity of causative lightning flashes considered. Noting that the peak lightning flash currents for the two cases considered here (Table 1) are more than ten times larger than the 10.53 kA peak current used in the work of Bortnik *et al.* [2006b], and the whistler wave magnetic field amplitude produced is directly proportional to the peak lightning current input into the model, the results are in good agreement. Consistent with Bortnik *et al.* [2006b], the majority ($>70\%$) of the energy flux is carried by 100–300 keV electrons.

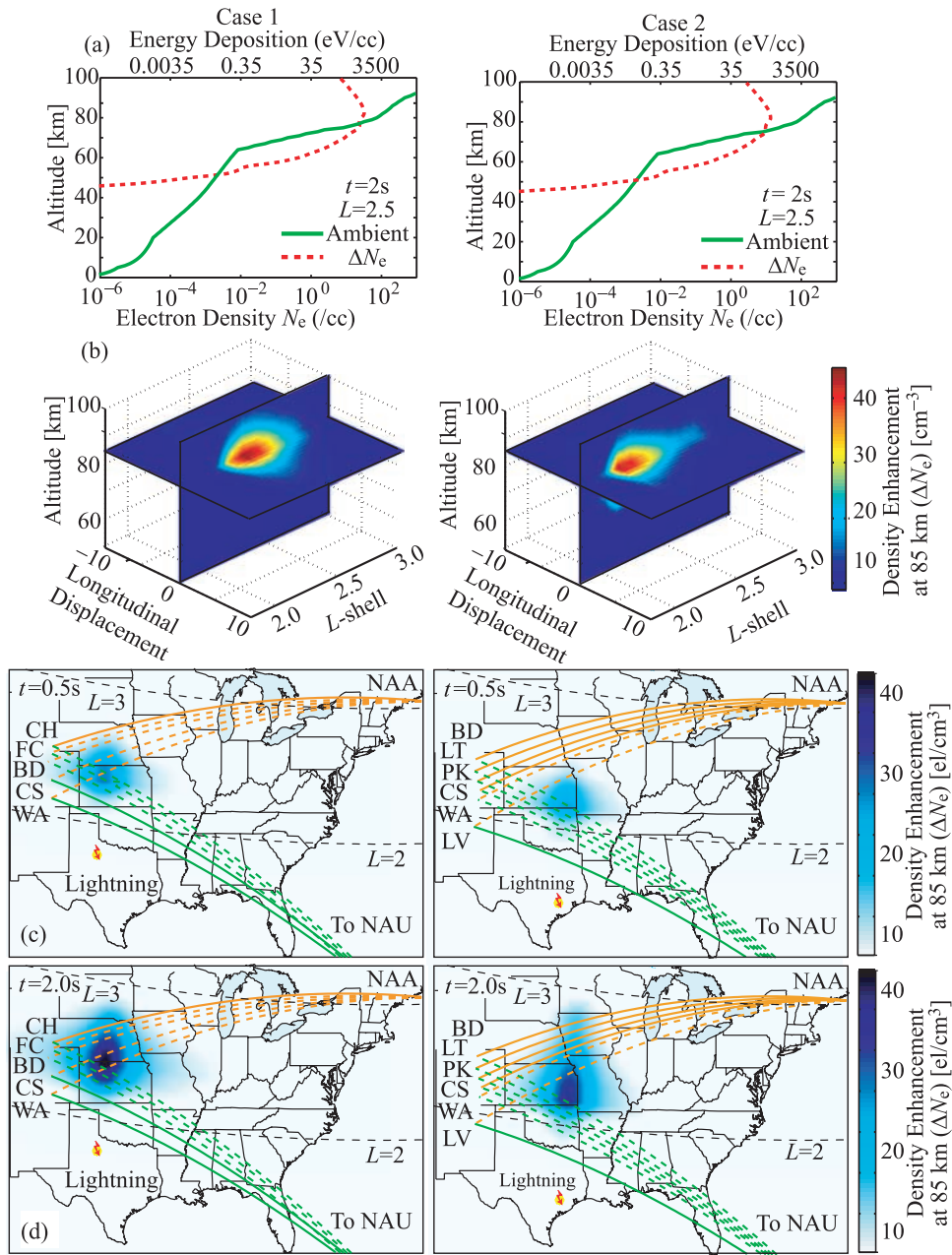


Figure 8. Energy deposition and density enhancement, showing (a) total energy deposited into the ionosphere, and resulting electron density enhancement, at $L = 2.5$ and $t = 2$ s for both cases. The disturbed ionospheric density profile is calculated by adding the electron density enhancement to the ambient ionospheric density profile (profile 2 in Figure 4 of *Pasko and Inan* [1994]). Also shown is (b) 3-D plot of electron density enhancement at $t = 2$ s. Two planes dissect the image at an altitude of 85 km and at 0° longitudinal displacement from the lightning source. Finally shown is (c) 2-D plot of electron density enhancement for both cases at $t = 0.5$ s and 85 km, superimposed on a map of the HAIL array and (d) 2-D plot of electron density enhancement at $t = 2$ s and 85 km, superimposed on a map of the HAIL array. The dashed lines represent GCPs on which a detectable perturbation is observed.

4.2. Energy Deposition and Electron Density Enhancement

[32] The time-integrated differential number flux (Figure 7b) is input into the Monte Carlo simulation of energy deposition (see section 3.2). The resulting energy deposition at $t = 2$ s and $L = 2.5$ as a function of altitude is shown in Figure 8a. The maximum in energy deposited is at ~ 85 km, the inferred

nighttime reflection height for VLF subionospheric signals. The resulting electron density enhancement is calculated assuming one ion-electron pair is produced per 35 eV deposited [Rees, 1963]. The peak density enhancement at ~ 85 km is $\sim 15\%$ of the ambient profile for both cases, consistent with previous modeling of ionospheric disturban-

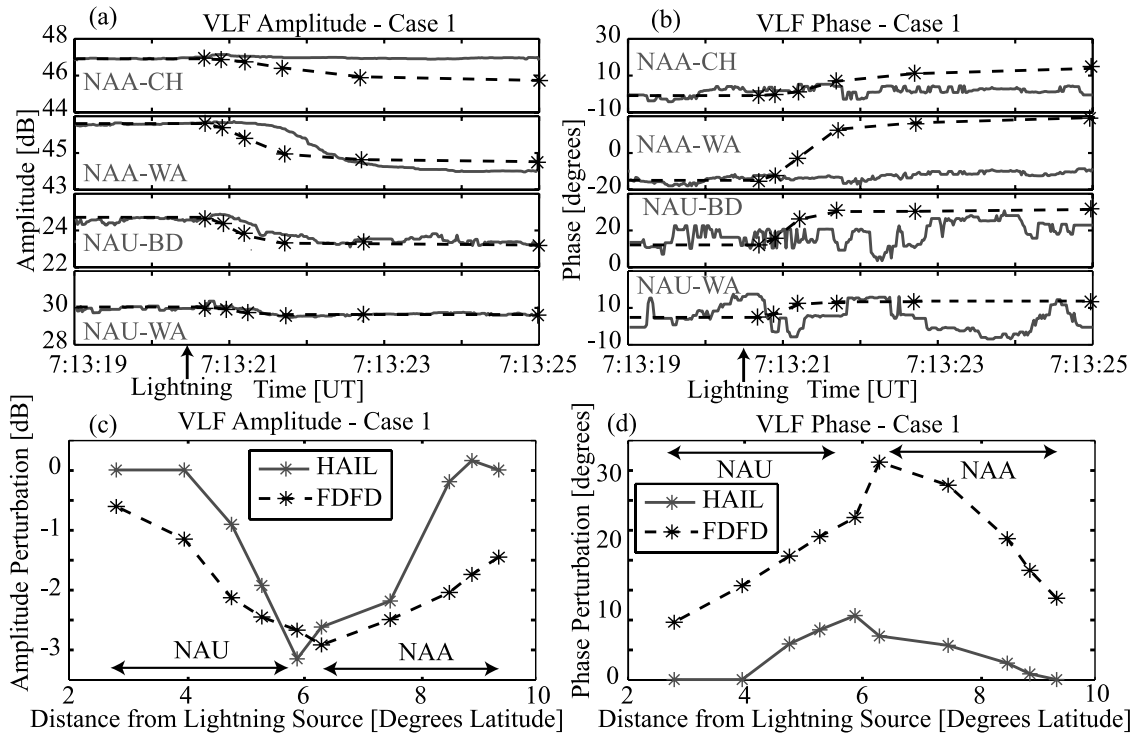


Figure 9. Comparison of modeled and observed VLF signal perturbations for Case 1, showing (a) a 6-s snapshot of four VLF signal amplitudes for Case 1, filtered with a 20-point median filter. The data from top to bottom relates to north to south GCPs. Overlaid in dashed lines are the VLF signal perturbations calculated by the model for Case 1 as a function of time. Also shown is (b) a 6-s snapshot of the observed and modeled phase for Case 1 and (c) observed (HAIL) and modeled (FDFD) amplitude perturbations of the VLF signal paths as a function of the distance from the lightning source at $t = 2$ s after the causative flash. Each asterisk denotes a separate VLF signal amplitude perturbation. The distance is measured from the flash location to the point of crossing of the GCP and the geomagnetic longitude of the causative flash. Finally shown is (d) the observed and modeled phase perturbations of the VLF signals for Case 1.

ces associated with LEP events [Clilverd *et al.*, 2002; Rodger *et al.*, 2002; Lev-Tov *et al.*, 1995].

[33] Figure 8b shows a three dimensional image of the time-integrated electron density enhancement as a function of L -shell, longitudinal displacement from the lightning source, and altitude. For both cases, the enhancement region is centered at ~ 85 km and at the longitude of the lightning flash. The enhancement region is peaked at higher L -shells in Case 1 ($L \sim 2.3$) than in Case 2 ($L \sim 2.1$), due to the different lightning source location.

[34] Taking the horizontal plane through the 3-D image gives the time-integrated density enhancement at 85 km (as a function of longitude and L -shell), which is superimposed on a map of the VLF signal paths (Figures 8c and 8d). As 85 km is near the VLF nighttime reflection height, the density enhancement at 85 km gives a reliable indication of the VLF perturbations expected for each HAIL path. The region of density enhancement agrees qualitatively with the perturbations observed on the HAIL array, with both the poleward displacement and spatial extent consistent with observations. This agreement suggests that the plasmaspheric density profile used in the model (Figure 5a) is similar to that in effect during the two cases. Comparison of the enhancement at $t = 0.5$ s and $t = 2$ s shows that the deposition of energy moves to higher L -shells with time, consistent with previous observations of nonducted LEP

events and the differential onset delay of the VLF perturbations observed [Peter and Inan, 2004].

4.3. VLF Signal Perturbation

[35] The FDFD model of VLF signal propagation (described in section 3.3) is used to quantitatively relate the ionospheric density enhancement to the VLF signal perturbations recorded at HAIL. The FDFD simulation is initially performed with an ambient ionospheric profile, giving an ambient amplitude and phase for each HAIL path. The disturbed ionospheric density profile (Figure 8) along the GCP is then input into the FDFD model, and the perturbed amplitude and phase is compared to the ambient amplitude and phase to determine the perturbation change in amplitude and phase. The perturbation in amplitude and phase calculated by the model is then directly compared to the HAIL VLF signal observations.

[36] Figures 9a, 9b, 10a, and 10b show 6-s snapshots of the VLF signal amplitude and phase recorded by HAIL. The time delay between the lightning flash and onset of perturbation increases with latitude, consistent with the effect previously referred to as “differential delay” [Peter and Inan, 2004]. Overlaid as asterisks are the VLF signal perturbations calculated by the model. The simulation results show a differential delay consistent with the observations. The event duration (as defined by Peter and Inan

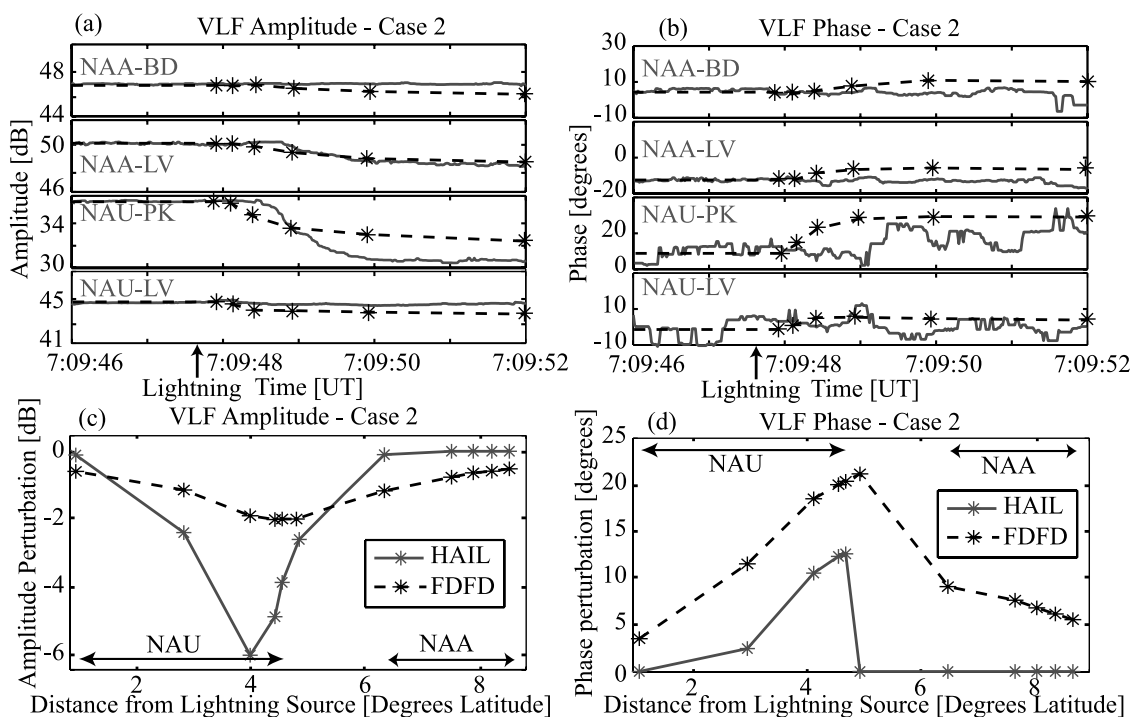


Figure 10. Comparison of modeled and observed VLF signal perturbations for Case 2, showing (a) a 6-s snapshot of the VLF signal amplitude recorded by HAIL for Case 2. Overlaid in dashed lines are the model calculations for the VLF signal perturbations. Also shown is (b) a 6-s snapshot of the VLF signal phase measured by HAIL and calculated by the model, (c) observed (HAIL) and modeled (FDFD) amplitude perturbations of the VLF signal paths as a function of the distance from the lightning source at $t = 2$ s, and (d) the observed and modeled phase perturbations of the VLF signals for Case 2.

[2004] and corresponding to the time over which significant precipitation occurs) calculated by the model is comparable to the VLF observations. However, the model has generally shorter onset delays (~ 0.5 s) than that observed in the HAIL data (~ 1 s).

[37] Past modeling work [Lauben *et al.*, 1999; Bortnik *et al.*, 2006a] has consistently calculated shorter onset delays than those observed for the two cases. Johnson *et al.* [1999] reported a number of LEP events detected by the HAIL array, with the causative lightning flashes located in the middle of Texas, and compared the perturbation signatures with a model of nonducted whistler-induced precipitation [Lauben *et al.*, 1999]. In order for the model and observation to agree, the modeled precipitation was delayed ~ 0.35 s in time, similar to the difference in onset delay between the observations and the model calculations of this work. Johnson *et al.* [1999] attributed this discrepancy to variations in the magnetospheric cold plasma density to values higher than those used in the work of Lauben *et al.* [1999], resulting in longer travel times for both the waves (whistler-mode refractive index is proportional to the square root of electron density) and particles (gyroresonant electron energies are lower for higher values of refractive index).

[38] While it is possible that the plasmaspheric cold plasma densities at the longitudes of the HAIL array are significantly higher than those used in the model (Figure 5a), we suggest here that another mechanism may be at least partly responsible for the discrepancy in onset

delay between the model results and observations. The number of particles at the edge of the northern bounce loss cone at the longitudes of the HAIL array is known to be substantially less than at the edge of the southern loss cone [Inan *et al.*, 1988, Figure 3]. Further, the wave-induced scattering involves small changes in pitch angle in comparison with the difference between the northern and southern loss cone angles [Bortnik *et al.*, 2002]. Hence the majority of the particles which are pitch-angle scattered during the first equatorial crossing of the whistler wave may be scattered into the southern bounce loss cone but not quite make it into the northern loss cone. These particles may thus not precipitate into the northern hemisphere directly. Instead, these particles would first mirror in the northern hemisphere and subsequently travel to the southern hemisphere where they would penetrate to lower mirror altitudes therein, colliding with atmospheric constituents [Inan *et al.*, 1988]. Since the particles nevertheless arrive at the southern hemisphere at grazing pitch angles (i.e., they have been barely moved into the southern loss cone) a significant fraction of these particles would in fact undergo “backscattering” upon collision in the southern atmosphere [Lehtinen, 2000, p. 90]. The particles’ pitch angle distribution would be broadened as a result of the backscattering interaction with the atmosphere. The particles would then return to the northern hemisphere, now having a more isotropic (i.e., broadened) pitch angle distribution. This more isotropic pitch angle distribution would include a

substantial number of particles within the northern loss cone, and the majority of these particles would then deposit their energy into the northern hemisphere atmosphere [Inan *et al.*, 1988].

[39] Compared to direct precipitation, these particles would undergo one full extra bounce period prior to precipitating, and so the onset delay between the lightning flash and the onset of the precipitation would be increased by ~ 0.4 s, consistent with the observations. For whistlers originating from northern hemisphere lightning, this mechanism would also result in shorter onset delays in the southern hemisphere than in the northern hemisphere, consistent with past observations [Burgess and Inan, 1990, Figure 5]. This mechanism would also result in substantially more precipitation in the southern than northern hemispheres, also consistent with past observations [Inan *et al.*, 1988].

[40] Figures 9c and 10c show the observed and modeled amplitude perturbations of the VLF signal paths as a function of the distance from the lightning source for both cases. The distance is measured from the flash location to the point of crossing of the GCP and the geomagnetic longitude of the causative flash. For the amplitude data for Case 1, the displacement of the peak perturbation from the causative flash is $\sim 6^\circ$ for the model and observation. The magnitude of the peak amplitude perturbation for the model and observation is within 25%. For Case 2, the displacement of the peak perturbation from the causative flash is $\sim 5^\circ$ for the simulation, $\sim 4^\circ$ for the HAIL observation. The magnitude of the peak perturbation is within a factor of three for Case 2, indicating that trapped flux levels may have increased during the second case. Clilverd *et al.* [2002] states that nonducted whistler-induced precipitation would occur with a 5° – 10° latitudinal gap between the lightning and the equatorward edge of the patch, inconsistent with the LEP events observed here. For the two cases examined here, this gap is far less (2° – 4°) and is dependent on the cold plasmaspheric density profile (section 3.1.1). The model calculates a perturbation region wider in latitudinal extent than what are observed for both Cases 1 and 2, the most likely reason being that the model assumes a slower falloff in the lightning-generated whistler wave energy with distance (see section 3) than what is actually generated by the lightning flashes in these cases.

[41] Given the variability in the trapped energetic flux (section 3.1.2), differences between the model and observation are expected. In fact, our main objective is not to achieve model calculations (for assumed trapped particle flux levels) that exactly match the HAIL VLF signal observations but is rather to develop metrics with which we can characterize the VLF signal perturbations in terms of the associated precipitation flux. In other words, it goes without saying that the trapped flux levels near the loss cone edge for any given case would not be known except in an average sense, and the knowledge of this quantity is not important for our purpose since precipitation flux is linearly proportional to trapped flux. The fact that the magnitude of the peak amplitude perturbations is within a factor of three of that observed on HAIL simply indicates that the trapped flux levels determined on the basis of the AE8 model and the POES measurements might have been reasonably representative for the cases.

[42] The model calculates positive phase perturbations, consistent with past work [Wolf and Inan, 1990] and the VLF signal perturbations detected on HAIL (Figures 9d and 10d). However, the model calculates phase perturbations consistently larger than those observed. The FDFD model calculates a ratio of ~ 0.1 [dB/deg] for amplitude and phase perturbations, smaller than that observed for the two cases by a factor greater than three. Inan and Carpenter [1987, equation (5)] theoretically estimated the ratio between amplitude and phase perturbations for a single mode VLF signal to be 0.048 [dB/deg], independent of the perturbation extent and intensity, even smaller than that calculated by the FDFD model.

[43] Starting at 0800 UT on 24 March 2001 (an hour after Case 1), phase perturbations on the scale calculated by the model are detected on the HAIL array that are associated with the same thunderstorm as Case 1. The amplitude signatures are similar to those of Case 1, so that the amplitude/phase ratio varied with time. The phase signatures of LEP events in HAIL data are generally less consistent (from event to event and from night to night) than the amplitude signatures, and are known to change over the course of a night by as much as an order of magnitude. Wolf and Inan [1990] examined VLF signatures of LEP events, and found only a weak correlation between amplitude and phase perturbations that is highly dependent on the path examined. The model does not accurately capture this variability in the VLF signal phase response. The reasons for this are not clear, but may indicate that the ambient ionospheric density profile used in the model was changing over the course of the night. This would result in a changing VLF signal reflection height with time and a corresponding change in the mode structure for the propagating VLF signal. The factors influencing the phase response of the VLF signal to precipitation events are suggested as an area that needs further analysis.

[44] It should also be noted that the VLF signal phase measured by HAIL is relatively noisy in comparison with the VLF signal amplitude, in part due to the fact that the MSK demodulation algorithm used in 2001 was a preliminary one. A more robust algorithm is currently in use at the HAIL VLF sites, providing substantially better signal-to-noise ratio for phase data. Given this fact, and knowing that the phase response varies considerably over time and for different paths, the VLF amplitude signatures recorded on HAIL for the two cases examined here give a more reliable measure of the ionospheric disturbance. With the recent installation of new hardware and software at the HAIL sites, the usability of the phase data for quantitative analysis is now much improved.

4.4. Metrics to Quantify LEP Events

[45] Given the variability in the trapped energetic flux (section 3.1.2), differences between the model and observation are expected. The trapped flux levels near the loss cone edge for any given case would not be known except in an average sense, and the knowledge of this quantity is not important for our purpose since precipitation flux is linearly proportional to trapped flux. The differences between the modeling results and the observed VLF signal perturbations are likely due to differences between the precipitation calculated by the model and the actual precipitation induced

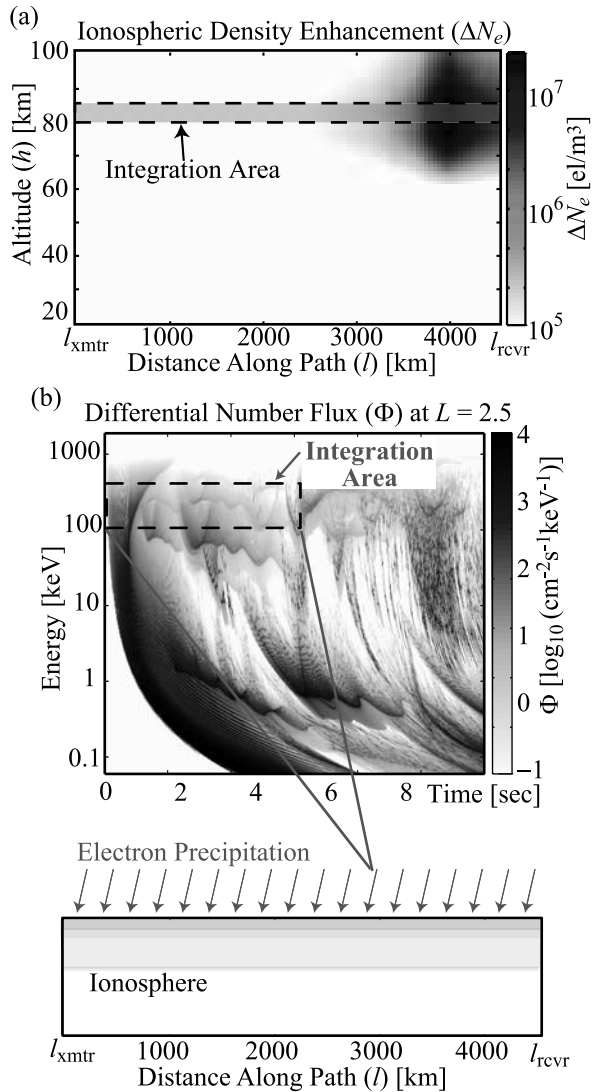


Figure 11. Illustration of metrics, showing (a) illustration of the integrated line density enhancement (N_{ILDE}) metric, as described in the text. The ionospheric electron density enhancement (ΔN_e) is shown as a function of altitude and distance along the path for a representative VLF signal path. The shaded box denotes the integration area from 80 to 85 km and over the path length. Also shown is (b) illustration of the precipitation metric Γ (section 4.4.2), with the top showing the precipitated differential number flux (Φ) at a representative location along a given signal path, repeated from Figure 7a. The boxed region denotes the integration area from 0 to 5 s and 100 to 300 keV in energy. The resulting precipitation is for a given location along the path, as represented at the bottom. The precipitation at each point along the path is calculated in a similar manner and integrated over the entire path length.

(due to uncertainties in the assumed near-loss-cone trapped flux levels). For the purposes of this section, we take the precipitation and ionospheric density enhancement calculated by the model as accurate, even though we know it is accurate only within the correlation of Figures 9 and 10. We assume that if the whistler-induced precipitation model

perfectly captured the precipitation, then the modeled VLF signal perturbations would show excellent agreement with the observations. There is currently no way to precisely measure either the precipitation or the trapped near-loss-cone flux, and hence the best we can do is to quantitatively relate the VLF signal perturbations to the modeled ionospheric density enhancement and electron precipitation.

[46] To quantitatively relate VLF signal perturbations to electron precipitation, two metrics are used to quantify the precipitation and ionospheric disturbance. Through comparison of the metrics with the VLF perturbations calculated by the FDFD model, quantitative relationships between VLF signal perturbations and the precipitation are estimated.

4.4.1. Integrated Line Density Enhancement (ILDE)

[47] The Integrated Line Density Enhancement (ILDE) metric gives a measure of the ionospheric density enhancement along a given VLF signal GCP. It is defined as the electron density enhancement produced by the energy deposition from the LEP event, integrated from 80 to 85 km in height and over the entire path length:

$$N_{ILDE} = \int_{80\text{km}}^{85\text{km}} \int_{l_{\text{xmtr}}}^{l_{\text{rcvr}}} \Delta N_e(l, h) dl dh \quad (1)$$

where l is the distance along the path, h is altitude, and ΔN_e is the electron enhancement obtained from the Monte Carlo simulation. N_{ILDE} has units of secondary electrons produced per meter perpendicular to the path.

[48] Figure 11a illustrates the calculation of N_{ILDE} for a given VLF signal path. The ionospheric electron density enhancement (ΔN_e) is calculated using the Monte Carlo model (section 3.2) as a function of distance along the VLF signal path. The density enhancement is then integrated from 80 to 85 km in altitude and along the entire VLF path length to obtain N_{ILDE} . As ΔN_e is obtained directly from the output of the Monte Carlo model of ionospheric density enhancement, N_{ILDE} provides an estimate of the expected VLF signal perturbation without having to use the FDFD model of VLF signal propagation. The FDFD model of VLF signal propagation currently requires the use of a supercomputer (due to the high memory requirements) and modeling a single VLF signal path takes several hours. Conversely, the metric N_{ILDE} can be calculated on a regular PC in less than a minute for a given VLF signal path.

[49] The validity of the ILDE metric is illustrated in Figures 12a and 12b, where N_{ILDE} is compared to the VLF signal perturbations calculated by the FDFD model as a function of distance from the lightning flash. As stated in section 4.4, differences between the FDFD model results and the VLF signal perturbations observed are expected due to the large variability in trapped energetic electron flux levels near the loss cone edge. We therefore compare N_{ILDE} directly to the VLF signal perturbations calculated by the model, assuming that the FDFD model calculations and the observations made on HAIL would agree if the inputs into the whistler-induced precipitation model were accurately known. The strong ($r > 0.9$) correlation indicates that N_{ILDE} does indeed give a reliable indication of the VLF signal perturbations expected.

[50] The strong correlation between the VLF signal perturbations calculated by the FDFD model and N_{ILDE}

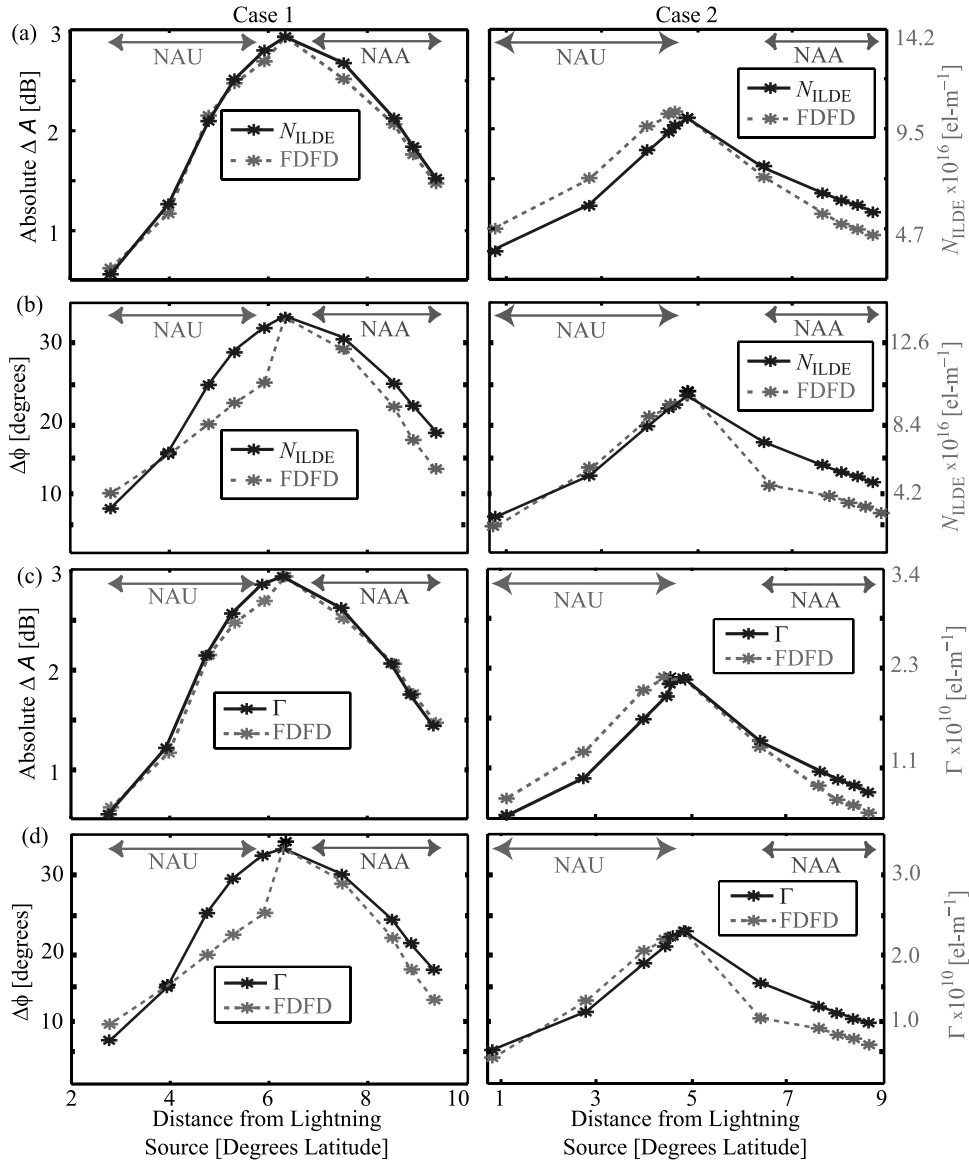


Figure 12. Metrics of disturbance for $t = 2$ s, showing (a) N_{ILDE} as a function of distance from the lightning source for both cases, with the scale shown on the right. Also shown is the VLF signal amplitude perturbation calculated by the FDFD model, with the scale shown to the left, (b) N_{ILDE} versus distance from the lightning source for both cases, compared to the VLF signal phase perturbation calculated by the model, (c) precipitation metric Γ (right axis) versus the modeled amplitude perturbation (left axis) as function of distance from the lightning flash for both cases, and (d) Γ compared to the modeled phase perturbation for both cases.

indicate that observations of VLF signal perturbations made on HAIL can be used to estimate the associated ionospheric density enhancement. To convert between the VLF amplitude perturbations observed on HAIL and the density enhancement along a given path, a conversion ratio α_{ILDE} of $5.1 \pm 1.8 \times 10^{16}$ [el m⁻¹/dB] is estimated for enhancement events of similar location and characteristics to the cases examined in this work, where $\alpha_{ILDE} = N_{ILDE}/\Delta A$. The ratio α_{ILDE} is determined by minimizing the mean square difference between $\alpha_{ILDE} \times \Delta A$ and N_{ILDE} for the LEP event magnitudes recorded for both cases on all VLF signal paths and at various times (over 50 points in total),

incorporating a range of density enhancements. The \pm indicates the range over which at least 70% (a single standard deviation) of the calculated metrics and the modeled VLF signal perturbations are correlated. The use of \pm is meant to denote this single standard deviation throughout the rest of this report and is assumed to give an indication of the uncertainty. The use of phase measurements to estimate the density enhancement is less reliable (section 4.3), and a conversion ratio β_{ILDE} of $5 \pm 2 \times 10^{15}$ [el m⁻¹/degree] should be used with caution, where $\beta_{ILDE} = N_{ILDE}/\Delta\phi$. Using these conversion ratios, VLF remote sensing can be used to infer the ionospheric density enhancement associ-

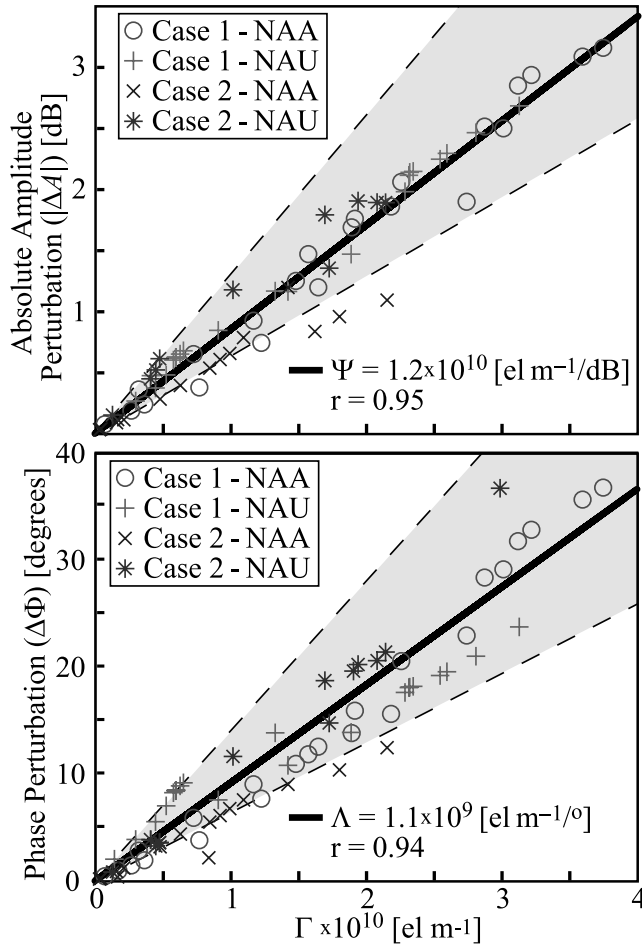


Figure 13. Scatterplots of Γ and VLF signal perturbations, showing (top) a scatterplot of the VLF amplitude perturbations calculated by the FDFD model as a function of Γ . Each point represents a particular VLF signal path at a particular time, with the case and transmitter signal denoted by different symbols. The slope of the solid black line equals the conversion ratio $\Psi = 1.2 \pm 0.3 \times 10^{10}$ [el m⁻¹/dB]. The shaded region denotes the range within which at least 70% of the points fall (one standard deviation) and corresponds to the \pm in Ψ . The amplitude perturbations are strongly correlated ($r > 0.9$) with Γ for both cases, both transmitters, and over a range of precipitation intensities. Also shown is (bottom) a scatterplot of the VLF phase perturbations calculated by the FDFD model as a function of Γ . The fitted line has a slope equal to the conversion ratio Λ of $1.1 \pm 0.4 \times 10^9$ [el m⁻¹/degree], with the shaded region denoting the range within at least 70% of the points fall.

ated with precipitation events, at least to the accuracy of Figures 9 and 10. These conversion ratios are suggested for precipitation events of similar location and characteristics, and for similar VLF path configurations, to the cases examined in this work. Application of this methodology to other types of precipitation events (and other VLF signal paths) should refine these conversion ratios to be applicable in other regions and on other VLF paths.

4.4.2. Electron Precipitation Metric (Γ)

[51] In order to quantitatively relate VLF signal perturbations directly to the energetic electron precipitation, we define a time-integrated precipitation metric Γ as follows:

$$\Gamma = \int_{l_{\text{kmr}}}^{l_{\text{evr}}} \int_{0\text{ s}}^{5\text{ s}} \int_{100\text{ keV}}^{300\text{ keV}} \Phi(E, t, l) dE dt dl \quad (2)$$

where E is electron energy, t is time of precipitation, and Φ is the precipitated differential number flux obtained from the whistler-induced precipitation model (section 4.1). The Γ metric has units of electrons precipitated per meter perpendicular to the path. Γ is defined in terms of the number of particles precipitated (rather than in terms of energy flux) to distinguish it from the metric N_{ILDE} and to relate it more closely to radiation belt electron loss.

[52] Figure 11b illustrates the calculation of Γ for a given VLF signal path. The precipitated differential number flux (Φ) at each point along the path is calculated using the whistler-induced precipitation model (section 3.2). Shown is the differential number flux at a representative location along the GCP, repeated from Figure 7a. The flux is then integrated from 0 to 5 s in time and 100 to 300 keV in energy to give the precipitation at a specific location along the path. This process is repeated at each location along the path (sampled every ~ 30 km), and integrated over the entire path length to obtain Γ . As Φ is obtained directly from the output of the whistler-induced precipitation model, Γ provides an estimate of the expected VLF signal perturbation without having to use either the FDFD model of VLF signal propagation or the Monte Carlo model of ionospheric density enhancement. For comparison, the initial Monte Carlo runs of energy deposition and density enhancement took several days to calculate. Conversely, the metric Γ is calculated in less than a minute for a given VLF signal path.

[53] In Figures 12c and 12d, Γ is compared to the VLF signal perturbations calculated by the FDFD model, as a function of distance from the lightning source. There is good agreement for both the NAA and NAU transmitter paths. This agreement is shown more clearly in Figure 13, a scatterplot of all the VLF signal perturbations calculated by the model as a function of Γ . The scatter plot includes all of the VLF signal paths over a range of times ($0 < t < 5$ s) and for both cases. While we examine only two representative LEP events, the results include a range of precipitation levels due to the modeling of several VLF signal paths at various times during the event onset (~ 50 points in total). Furthermore, the two case studies are representative of LEP events that occurred on the nights of 24 and 28 March 2001 (~ 70 LEP events on each night), which were caused by lightning of similar location and that showed similar LEP event signatures [Peter and Inan, 2004].

[54] The strong ($r > 0.9$) correlation indicates that Γ provides a reliable indication of the VLF signal perturbations expected, and that observations of VLF signal perturbations made on HAIL can be used to estimate the associated electron precipitation along a given GCP. A conversion ratio Ψ of $1.2 \pm 0.3 \times 10^{10}$ [el m⁻¹/dB] is estimated for precipitation events of similar location and characteristics (and similar VLF path configurations) to the cases examined in this work, with $\Psi = \Gamma/\Delta A$. The conver-

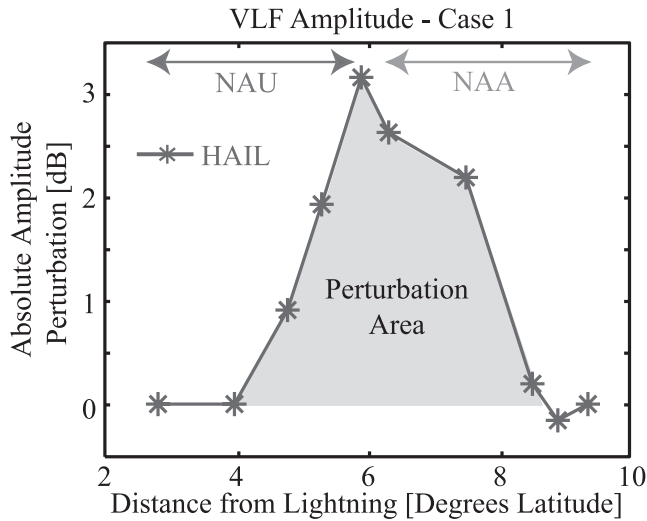


Figure 14. Perturbation area, showing HAIL observations of the absolute amplitude perturbation as a function of latitudinal distance from the lightning flash for Case 1, repeated from Figure 9c. The shaded area represents the perturbation area, integrated over latitude, used to estimate the total precipitation (Υ) induced by the Case 1 lightning flash (100–300 keV).

sion ratio Ψ is equal to the slope of the black line shown in Figure 13 (top) and is calculated in the same manner as α_{ILDE} . The use of phase measurements to estimate precipitation is less reliable, and a conversion ratio Λ of $1.1 \pm 0.4 \times 10^9$ [el m⁻¹/degree] should be used with caution, with $\Lambda = \Gamma/\Delta\phi$. The shaded region denotes the range within which at least 70% of the points fall (one standard deviation) and corresponds to the \pm used for Ψ and Λ .

[55] It should be noted that the conversion ratios (α_{ILDE} and Ψ) establish a linear relationship between our metrics (N_{ILDE} and Γ) and a logarithmic quantity, the VLF signal amplitude perturbation measured in decibels. However, given the small range of amplitude perturbations examined in this work and typically associated with LEP events, the amplitude perturbation measured in dB behaves in a nearly linear fashion, and hence we can establish a linear relationship between our metrics and the amplitude perturbations measured in dB. Using these ratios, VLF remote sensing can be used to quantitatively estimate the precipitation associated with LEP events, without the need to input trapped electron flux levels, as demonstrated in the next section.

4.4.3. Estimating Precipitation From VLF Data

[56] Figure 4 shows a block diagram illustrating the relationship of the metrics and associated conversion ratios to the model framework. Developed with respect to the LEP model, the conversion ratios allow us to use VLF signal perturbations observed on HAIL to infer the electron precipitation and ionospheric disturbance associated with a given lightning flash. We now demonstrate the use of these conversion ratios for the two case lightning flashes.

[57] Using Ψ , VLF data can be used to quantitatively estimate the total precipitation loss associated with a LEP event. Assuming the HAIL paths are oriented in the east-west direction, so that integrating across the paths is

equivalent to an integral over latitude, the total number of electrons precipitated (100–300 keV) for a LEP event (Υ) is estimated as follows:

$$\Upsilon \simeq (1.1 \times 10^5) \times \Psi \times \int_{\lambda_0}^{\lambda_1} |\Delta A(\lambda)| d\lambda \quad (3)$$

where ΔA is the amplitude perturbation (in dB), Ψ is the conversion ratio previously obtained and equals $1.2 \pm 0.3 \times 10^{10}$ [el m⁻¹/dB], the factor 1.1×10^5 is used to convert from degrees latitude to meters, and λ is the latitudinal distance from the lightning flash to the GCP. As illustrated in Figure 14, integrating the HAIL VLF signal perturbations for Case 1 (Figure 9c) over latitude gives a perturbation area of 1.46×10^6 [dB-m]. Multiplying the perturbation area by Ψ gives a total electron precipitation (100–300 keV) induced by the LEP event of $1.8 \pm 0.4 \times 10^{16}$ electrons. Similarly, a perturbation area of 0.98×10^6 [dB-m] for Case 2 gives a total loss of $1.2 \pm 0.3 \times 10^{16}$ electrons (100–300 keV). This estimate of precipitation loss is calculated directly from the VLF signal perturbations observed on HAIL, using only the conversion ratio Ψ .

[58] It should be noted that what we refer to as precipitation here includes all particles scattered into the bounce loss cone (as defined in Γ and Ψ). For example, if only 50% of the particles which are scattered into the northern bounce loss cone deposit their energy into the atmosphere (with the remaining 50% mirroring and/or backscattering instead), the actual number of electrons depositing their energy into the northern hemisphere atmosphere for a given observed VLF signal perturbation is actually a factor of two less than that estimated by the conversion ratio Ψ . Therefore the conversion ratio Ψ should be considered an upper bound when used in estimating the number of particles precipitated as the ratio is used to estimate the total number of particles scattered into the bounce loss cone. As the relative roles of direct versus backscattered precipitation and the evolution of the pitch angle distribution of scattered particles within the loss cone over time are more clearly understood, the definitions of Γ and Ψ may need to be refined.

[59] Following this methodology, subionospheric VLF data can provide a quantitative measure of the loss of energetic electrons into the atmosphere. This estimate furthermore does not require assumptions regarding the trapped near-loss-cone pitch angle distribution and flux levels in the radiation belt, as the estimate of precipitation is calculated directly from the conversion ratio Ψ and VLF signal observations. It should be noted that the metrics presented are for nonducted LEP events detected by the HAIL array. Similar analysis to that presented here, applied to other precipitation events and other VLF paths, should broaden the use of VLF remote sensing to quantitatively estimate precipitation on a global scale. This methodology is fully applicable to other types of precipitation events and other VLF signal path configurations, the values of the conversion ratios (i.e., Ψ and α_{ILDE}) simply need to be recalculated for the particular case considered. Any lack of correlation of the metrics defined herein with VLF signal perturbations in other precipitation events would likely be due either to the energy spectra of precipitation and/or the ambient ionospheric density profile along the VLF signal

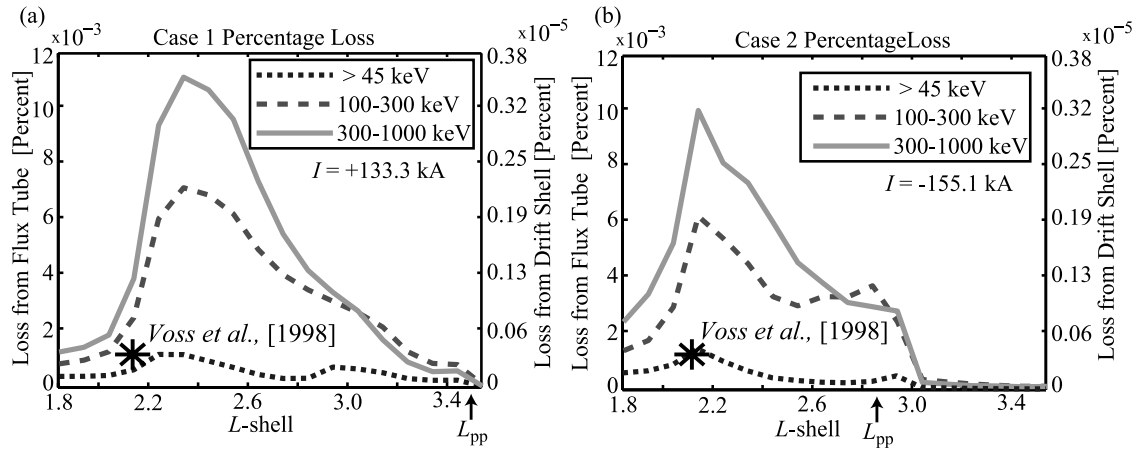


Figure 15. Particle loss, showing (a) percentage of electrons lost into the bounce loss cone from a single flux tube at the geomagnetic longitude of the lightning flash, as a function of L -shell, for three energy ranges and Case 1. The scale on the right shows the percentage loss (integrated over longitude) from the drift shell (calculated over the entire drift orbit, assuming an azimuthally independent trapped flux). This value represents the percentage of all available trapped particles, as a function of L -shell, lost by a single lightning flash. Also shown is (b) percentage of electrons lost for Case 2. Also shown is the peak current of the lightning flash (I) for both cases. The asterisks show the calculation of precipitation loss from *Voss et al.* [1998].

path being substantially different than that assumed for the cases analyzed here. A similar methodology to that presented here has already been successfully applied to sub-ionospheric VLF signatures of VLF transmitter-induced precipitation [*Inan et al.*, 2007a], and further refinements of the conversion ratios should encourage the use of VLF remote sensing to quantitatively measure precipitation events.

5. Conclusions

[60] On the basis of the low-altitude S81-1 (SEEP) satellite measurement of LEP events, *Voss et al.* [1998] calculated that $\sim 0.0015\%$ of $E > 45$ keV electrons in a single flux tube at $L = 2.15$ were precipitated in a single LEP event. The precipitation was assumed to be due to ducted whistlers, although no independent evidence existed for the ducted nature of the interaction. Using *Voss et al.* [1998, equation (5)], we calculate the percentage loss from a single flux tube at the geomagnetic longitude of the lightning flash, for a range of L -shells (Figure 15). The number of electrons in a magnetic flux tube is calculated by integrating the differential directional flux over solid angle, energy, and a full bounce period. The trapped flux is obtained from the AE8-radiation belt model (section 3.1.2) and the precipitation flux is obtained from the whistler-induced precipitation model results (section 4.1). The percentage loss is independent of the trapped flux levels input into the model (as the precipitation flux is approximately proportional to the trapped flux levels) but does depend on the initial pitch angle distribution. The loss includes all particles scattered into the northern and southern bounce loss cones. As we do not have VLF signal perturbation measurements in the conjugate location in the southern hemisphere for the two cases examined, we can only verify the precipitation in the northern hemisphere. Again, we define precipitation loss here as all particles scattered into the bounce loss cone, while not all of

these particles may in fact deposit their energy into the atmosphere (i.e., some particles may instead mirror and/or backscatter). Hence the loss estimates given here should be considered an upper bound.

[61] For Case 1, the percentage loss from a single flux tube (for 100–300 keV) peaks at $\sim 0.007\%$ at $L \sim 2.35$. For Case 2 the percentage loss peaks at $\sim 0.006\%$ at $L \sim 2.2$. Notice the secondary peak at $L \sim 2.8$ in Case 2, due to the guiding of whistler wave energy near the plasmapause [*Inan and Bell*, 1977]. To compare with *Voss et al.* [1998], the percentage loss for $E > 45$ keV is also shown. For Case 1, the percentage loss peaks at $\sim 0.001\%$ at $L \sim 2.3$. For Case 2, the loss peaks at $\sim 0.0015\%$ at $L \sim 2.15$. The excellent agreement between the model and *Voss et al.* [1998] adds credence to the accuracy of the model and our metrics, at least for the L -shell range and the VLF path distribution of the HAIL array. Also shown (right axis) is the percentage of total flux lost (integrated over longitude) from the drift shell (calculated over the entire drift shell). The loss as a function of longitude is simply a scaling function times the peak loss (section 3.1), and hence the loss at each L -shell integrated over longitude is simply a constant times the peak loss at the longitude of the lightning flash. Since we are assuming no azimuthal variations in trapped flux, the trapped flux integrated over longitude is also a constant for each L -shell. Therefore the percentage drift shell loss is simply the percentage loss from a single flux tube at the lightning longitude times a scaling factor (~ 0.0319).

[62] The modeling framework presented in this report is the most comprehensive model to date in terms of quantitative interpretation of VLF signal perturbations associated with nonducted lightning-induced electron precipitation. The precipitation calculated by the model is highly dependent on the trapped near-loss-cone radiation belt flux levels assumed, and hence our main objective is not to compare model calculations with the HAIL VLF signal observations

on an absolute basis but is rather to develop metrics with which we can characterize the VLF signal perturbations in terms of the associated precipitation flux. While the main purpose of this report is to demonstrate the method by which VLF signal perturbations can be quantitatively related to the causative electron precipitation, the comparison of the model results with the VLF signal observations reveal some enlightening discrepancies between the current model and the HAIL observations. First, the model predictions suggest onset delays significantly shorter than those observed, suggesting the electrons precipitating in the north may have first backscattered in the southern hemisphere. Second, the model predictions suggest a region of disturbance of greater spatial extent than that observed, indicating that the whistler wave illumination region used in the model may need to be refined. Third, the observed VLF signal phase response varies significantly over a given night and from day to day. The model fails to accurately capture the variable phase response of the VLF signal to the precipitation.

[63] We have introduced two metrics (N_{ILDE} and Γ) that give an estimate of the electron precipitation ionospheric density enhancement represented by VLF signal perturbations observed with the HAIL array. The robustness of these metrics for the case in hand is a result of several factors, including: (1) the ionospheric disturbance is smoothly varying throughout the region of interest; (2) the VLF signal at the location of the receivers is relatively stable (Figure 6d); (3) the energy spectra of the precipitation does not vary dramatically with time or location; and (4) the location of the precipitation along each VLF signal path is similar for all GCPs and for both cases. The correlation between the metrics and the VLF signal perturbations suggest the use of conversion ratios (α_{ILDE} and Ψ) to quantitatively relate VLF signal perturbations to the causative ionospheric disturbance and electron precipitation. These conversion ratios are suggested for precipitation events of similar location and characteristics to the cases examined in this work. For a given lightning flash location, the model predicts an approximately linear dependence of the precipitation flux on the source lightning current and the trapped radiation belt flux levels. However, this linearity has not yet been examined on a statistical basis for observed LEP events. A broader survey of events would help explore the relationship between LEP event magnitude and the source lightning current and trapped flux levels, and would help refine the metrics and conversion ratios to be applicable to other precipitation events and other regions.

[64] The recent work of *Inan et al.* [2007b] documented observations of LEP activity as detected by the DEMETER satellite. The whistler-induced precipitation model used in this report was applied to those events and estimated precipitation flux and energy spectra consistent with the observations, supporting the validity of the model framework used in this report.

[65] *Abel and Thorne* [1998a, 1998b] theoretically estimated the loss rates of radiation belt electrons from 100 to 1500 keV due to Coulomb collisions and resonant interactions with plasma waves, including plasmaspheric hiss, lightning-generated whistlers, and VLF transmitters. Owing to their ease of installation and continuous time coverage, the use of ground-based VLF receivers to quantitatively

measure precipitation events can provide an excellent experimental verification of the theoretical work of *Abel and Thorne* [1998a, 1998b] and *Bortnik et al.* [2003a]. This report demonstrated a methodology for quantitatively relating VLF signal perturbations to the causative precipitation, and encourages the use of VLF remote sensing in the quantitative analysis of electron precipitation events.

[66] **Acknowledgments.** This work was supported by the National Science Foundation under grants ATM-9910532 and ATM-0551174 and the Office of Naval Research under grant N00014-03-1-0333. The authors especially thank Michael Chevalier for his help with the FDFD model and Monte Carlo simulation. The running of the VLF signal propagation model was supported in part by the National Science Foundation through the San Diego Supercomputer Center under grants ATM060010 and ATM060017T using the DATASTAR Teragrid. We also thank Jacob Bortnik for his assistance with the WIPPB model, as well as Nikolai Lehtinen, Timothy Chevalier, and Maria Spasojevic for their help. The authors thank the many high school teachers and students involved in the support of the HAIL array. We also thank Ken Cummins of Vaisala for the use of NLDN data. [67] Zuyin Pu thanks Michael J. Starks and another reviewer for their assistance in evaluating this paper.

References

- Abel, B., and R. M. Thorne (1998a), Electron scattering loss in Earth's inner magnetosphere: 1. Dominant physical processes, *J. Geophys. Res.*, *103*, 2385.
- Abel, B., and R. M. Thorne (1998b), Electron scattering loss in Earth's inner magnetosphere: 2. Sensitivity to model parameters, *J. Geophys. Res.*, *103*, 2397.
- Angerami, J. J., and J. O. Thomas (1964), Studies of planetary atmospheres. 1. Distribution of electrons + ions in earths exosphere, *J. Geophys. Res.*, *69*, 4537.
- Banks, P. M., C. R. Chappell, and A. F. Nagy (1974), A new model for the interaction of auroral electrons with the atmosphere: Spectral degradation, backscatter, optical emissions, and ionization, *J. Geophys. Res.*, *79*, 1459.
- Bell, T. F. (1984), The nonlinear gyroresonance interaction between energetic electrons and coherent VLF waves propagating at an arbitrary angle with respect to the Earth's magnetic-field, *J. Geophys. Res.*, *89*, 905.
- Bell, T. F., U. S. Inan, J. Bortnik, and J. D. Scudder (2002), Landau damping of magnetospherically reflected whistlers within the plasmasphere, *Geophys. Res. Lett.*, *29*(15), 1733, doi:10.1029/2002GL014752.
- Blake, J. B., U. S. Inan, M. Walt, T. F. Bell, J. Bortnik, D. L. Chenette, and H. J. Christian (2001), Lightning-induced energetic electron flux enhancements in the drift loss cone, *J. Geophys. Res.*, *106*, 29,733.
- Bortnik, J. (2004), Precipitation of radiation belt electrons by lightning-generated magnetospherically reflecting whistler waves, thesis, Stanford Univ., Stanford, Calif.
- Bortnik, J., U. S. Inan, and T. F. Bell (2002), L dependence of energetic electron precipitation driven by magnetospherically reflecting whistler waves, *J. Geophys. Res.*, *107*(A8), 1150, doi:10.1029/2001JA000303.
- Bortnik, J., U. S. Inan, and T. F. Bell (2003a), Energy distribution and lifetime of magnetospherically reflecting whistlers in the plasmasphere, *J. Geophys. Res.*, *108*(A5), 1199, doi:10.1029/2002JA009316.
- Bortnik, J., U. S. Inan, and T. F. Bell (2003b), Frequency-time spectra of magnetospherically reflecting whistlers in the plasmasphere, *J. Geophys. Res.*, *108*(A1), 1030, doi:10.1029/2002JA009387.
- Bortnik, J., U. S. Inan, and T. F. Bell (2006a), Temporal signatures of radiation belt electron precipitation induced by lightning-generated MR whistler waves: 1. Methodology, *J. Geophys. Res.*, *111*, A02204, doi:10.1029/2005JA011182.
- Bortnik, J., U. S. Inan, and T. F. Bell (2006b), Temporal signatures of radiation belt electron precipitation induced by lightning-generated MR whistler waves: 2. Global signatures, *J. Geophys. Res.*, *111*, A02205, doi:10.1029/2005JA011398.
- Brinca, A. L. (1972), On the stability of obliquely propagating whistlers, *J. Geophys. Res.*, *77*, 3495.
- Burgess, W. C., and U. S. Inan (1990), Simultaneous disturbance of conjugate ionospheric regions in association with individual lightning flashes, *Geophys. Res. Lett.*, *17*, 259.
- Burgess, W. C., and U. S. Inan (1993), The role of ducted whistlers in the precipitation loss and equilibrium flux of radiation belt electrons, *J. Geophys. Res.*, *98*, 15,643.
- Carpenter, D. L., and R. R. Anderson (1992), An ISEE/whistler model of equatorial electron density in the magnetosphere, *J. Geophys. Res.*, *97*, 1097.

- Chevalier, M. W., and U. S. Inan (2006), A technique for efficiently modeling long path propagation for use in both FDFD and FDTD, *IEEE Antennas Wireless Propag. Lett.*, *5*, 525, doi:10.1109/LAWP.2006.887551.
- Ciliverd, M. A., D. Nunn, S. J. Lev-Tov, U. S. Inan, R. L. Dowden, C. J. Rodger, and A. J. Smith (2002), Determining the size of lightning-induced electron precipitation patches, *J. Geophys. Res.*, *107*(A8), 1168, doi:10.1029/2001JA000301.
- Cummins, K. L., M. J. Murphy, E. A. Bardo, W. L. Hiscox, R. B. Pyle, and A. E. Pifer (1998), A combined TOA/MDF technology upgrade of the U.S. National Lightning Detection Network, *J. Geophys. Res.*, *103*, 9035.
- Glukhov, V. S., V. P. Pasko, and U. S. Inan (1992), Relaxation of transient lower ionospheric disturbances caused by lightning-whistler-induced electron precipitation bursts, *J. Geophys. Res.*, *97*, 16,971.
- Green, J. L., S. Boardsen, L. Garcia, W. W. L. Taylor, S. F. Fung, and B. W. Reinisch (2005), On the origin of whistler mode radiation in the plasmasphere, *J. Geophys. Res.*, *110*, A03201, doi:10.1029/2004JA010495.
- Haselgrove, J. (1954), Ray theory and a new method for ray tracing, paper presented at Conference on Physics of the Ionosphere, Phys. Soc., Cambridge, U. K.
- Helliwell, R. A. (1965), *Whistlers and Related Ionospheric Phenomena*, Stanford Univ. Press, Stanford, Calif.
- Helliwell, R. A., J. P. Katsufakis, and M. L. Trimpi (1973), Whistler-induced amplitude perturbation in VLF propagation, *J. Geophys. Res.*, *78*, 4679.
- Inan, U. S., and T. F. Bell (1977), The plasmopause as a VLF wave guide, *J. Geophys. Res.*, *83*, 2819.
- Inan, U. S., and D. L. Carpenter (1986), On the correlation of whistlers and associated subionospheric VLF/LF perturbations, *J. Geophys. Res.*, *91*, 3106.
- Inan, U. S., and D. L. Carpenter (1987), Lightning-induced electron precipitation events observed at $L = 2.4$ as phase and amplitude perturbations on subionospheric VLF signals, *J. Geophys. Res.*, *92*, 3293.
- Inan, U. S., T. F. Bell, and H. C. Chang (1982), Particle-precipitation induced by short-duration VLF waves in the magnetosphere, *J. Geophys. Res.*, *87*, 6243.
- Inan, U. S., D. L. Carpenter, R. A. Helliwell, and J. P. Katsufakis (1985), Subionospheric VLF/LF phase perturbations produced by lightning-whistler induced particle precipitation, *J. Geophys. Res.*, *90*, 7457.
- Inan, U. S., T. G. Wolf, and D. L. Carpenter (1988), Geographic distribution of lightning-induced electron precipitation observed as VLF/LF perturbation events, *J. Geophys. Res.*, *93*, 9841.
- Inan, U. S., M. Walt, H. Voss, and W. Imhof (1989), Energy spectra and pitch angle distribution of lightning-induced electron precipitation: analysis of an event observed on the S81-1 (SEEP) satellite, *J. Geophys. Res.*, *94*, 1379.
- Inan, U. S., M. Golkowski, M. K. Casey, R. C. Moore, W. Peter, P. Kulkarni, P. Kossey, and E. Kennedy (2007a), Subionospheric VLF observations of transmitter-induced precipitation of inner radiation belt electrons, *Geophys. Res. Lett.*, *34*, L02106, doi:10.1029/2006GL028494.
- Inan, U. S., D. Piddychiy, W. B. Peter, T. F. Bell, J. A. Sauvaud, and M. Parrot (2007b), DEMETER satellite observations of lightning-induced electron precipitation bursts, *Geophys. Res. Lett.*, *34*, L07103, doi:10.1029/2006GL029238.
- Jasna, D. (1993), Gyroresonant scattering of radiation belt electrons by oblique whistler waves, thesis, Stanford Univ., Stanford, Calif.
- Johnson, M. P., U. S. Inan, and D. S. Lauben (1999), Subionospheric VLF signatures of oblique (nonducted) whistler-induced precipitation, *Geophys. Res. Lett.*, *26*, 3569.
- Lauben, D. S., U. S. Inan, and T. F. Bell (1999), Poleward-displaced electron precipitation and lightning-generated oblique whistlers, *Geophys. Res. Lett.*, *26*, 2633.
- Lee, J. H., and D. K. Kalluri (1999), Three-dimensional FDTD simulation of electromagnetic wavetransformation in a dynamic inhomogeneous magnetized plasma, *IEEE Trans. Antennas Propag.*, *47*, 7.
- Lehtinen, N. G. (2000), Relativistic runaway electrons above thunderstorms, thesis, Stanford Univ., Stanford, Calif.
- Lehtinen, N. G., U. S. Inan, and T. F. Bell (2001), Effects of thunderstorm-driven runaway electrons in the conjugate hemisphere: Purple sprites, ionization enhancements, and gamma rays, *J. Geophys. Res.*, *106*, 28,841.
- Lev-Tov, S. J., U. S. Inan, and T. F. Bell (1995), Altitude profiles of localized D region density disturbances produced in lightning-induced electron precipitation events, *J. Geophys. Res.*, *100*, 21,375.
- Park, C. G. (1972), Methods of determining electron concentrations in the magnetosphere from nose whistlers, *Tech. Rep. 3454-1*, Stanford Univ., Stanford, Calif.
- Pasko, V. P., and U. S. Inan (1994), Recovery signatures of lightning-associated VLF perturbation as a measure of the lower ionosphere, *J. Geophys. Res.*, *99*, 17,523.
- Peter, W. B., and U. S. Inan (2004), On the occurrence and spatial extent of electron precipitation induced by oblique nonducted whistler waves, *J. Geophys. Res.*, *109*, A12215, doi:10.1029/2004JA010412.
- Poulsen, W. L., T. F. Bell, and U. S. Inan (1993), The scattering of VLF waves by localized ionospheric disturbances produced by lightning-induced electron precipitation, *J. Geophys. Res.*, *98*, 15,553.
- Rees, M. H. (1963), Auroral ionization and excitation by incident energetic electrons, *Planet. Space Sci.*, *11*, 1209.
- Rodger, C. J., M. A. Ciliverd, and R. L. Dowden (2002), D region reflection height modification by whistler-induced electron precipitation, *J. Geophys. Res.*, *107*(A7), 1145, doi:10.1029/2001JA000311.
- Rodger, C. J., D. Nunn, and M. A. Ciliverd (2004), Investigating radiation belt losses through numerical modeling of precipitating fluxes, *Ann. Geophys.*, *22*, 3657.
- Taflove, A., and S. C. Hagness (2000), *Computational Electrodynamics: The Finite Difference Time-Domain Method*, Artech House, Boston.
- Tarcsai, G., P. Szemeredy, and L. Hegymegi (1988), Average electron density profiles in the plasmasphere between $L = 1.4$ and 3.2 deduced from whistlers, *J. Atmos. Terr. Phys.*, *50*, 607.
- Thorne, R. M., and R. B. Horne (1994), Landau damping of magnetospherically reflected whistlers, *J. Geophys. Res.*, *99*, 17,249.
- Uman, M. A. (1984), *Lightning*, Dover, Mineola, N. Y.
- Vette, J. (1991), The AE-8 trapped electron model environment, *Rep. 91-24*, Natl. Space Sci. Data Cent., Greenbelt, Md.
- Voss, H. D., M. Walt, W. L. Imhof, J. Mobilia, and U. S. Inan (1998), Satellite observations of lightning-induced electron precipitation, *J. Geophys. Res.*, *103*, 11,725.
- Wait, J. R., and K. P. Spies (1964), Characteristics of the Earth-ionosphere waveguide for VLF radio waves, *Tech. Note 300*, Natl. Bur. of Stand., Boulder, Colo.
- Walt, M. (1994), *Introduction to Geomagnetically Trapped Radiation*, Cambridge Univ. Press, New York.
- Wolf, T. G., and U. S. Inan (1990), Path-dependent properties of subionospheric VLF amplitude and phase perturbations associated with lightning, *J. Geophys. Res.*, *95*, 20,997.

U. S. Inan and W. B. Peter, Space Telecommunications and Radioscience Laboratory, Stanford University, 308 Packard Building, Stanford, CA 94305, USA. (wpeter@stanford.edu)